

A Large-Volume Scintillation Detector for the Study of Cosmic-Ray Muons

---

A Thesis  
Presented to  
The Division of Mathematics and Natural Sciences  
Reed College

---

In Partial Fulfillment  
of the Requirements for the Degree  
Bachelor of Arts

---

Neal Dawson Woo

May 2015



Approved for the Division  
(Physics)

---

John Essick



# Acknowledgements

First and foremost, I wish to thank John Essick for his guidance and encouragement throughout the thesis process, without whom none of this would have been possible. I could not imagine having had a better adviser.

I must also thank my parents for always being supportive of me since before I can remember. You have taught me much more than I could ever write down in a thesis. I love you!

Eileen- you have always believed in me, even when I didn't believe in me. I am so happy to have shared this year with you.

Lastly, I must thank this beautiful place and all of these wonderful people for shaping me into who I am today. It has been unforgettable!



# Table of Contents

<b>Introduction</b> . . . . .	<b>1</b>
<b>Chapter 1: Fermi's Theory of Muon Decay</b> . . . . .	<b>5</b>
1.1 Relativistic Kinematics . . . . .	8
1.2 Dirac Particles . . . . .	10
1.3 The Feynman Calculus for Weak Interactions . . . . .	16
1.4 Decay of the Muon . . . . .	19
<b>Chapter 2: The Physics of Scintillation Detectors</b> . . . . .	<b>27</b>
2.1 Passage of Radiation through Matter . . . . .	27
2.1.1 The Bethe-Bloch Formula . . . . .	29
2.1.2 Energy Loss of Electrons and Positrons . . . . .	32
2.1.3 NIST EStar Database . . . . .	34
2.1.4 The Landau-Vavilov Distribution . . . . .	35
2.2 Scintillation . . . . .	37
2.3 Photomultiplier Tubes . . . . .	40
2.3.1 The Photocathode . . . . .	41
2.3.2 Electron Multiplier . . . . .	42
2.3.3 Single-Photoelectron Statistics . . . . .	43
<b>Chapter 3: Detector Design and Experimental Procedure</b> . . . . .	<b>45</b>
3.1 Apparatus . . . . .	45
3.2 Data Acquisition in NI LabVIEW . . . . .	48
3.3 Monte Carlo Method . . . . .	49
3.3.1 Particle Tracking and Transport . . . . .	50
3.3.2 Hard Interactions . . . . .	51
3.3.3 Soft Interactions . . . . .	54
3.3.4 Simulation Logic . . . . .	56
<b>Chapter 4: Results and Analysis</b> . . . . .	<b>59</b>
4.1 Pulse Processing & Integration . . . . .	59
4.2 Energy Distributions . . . . .	60
4.2.1 Weak Pulses . . . . .	61
4.2.2 High-energy Anomalies . . . . .	62
4.3 Measurement of $m_\mu$ . . . . .	65

4.4 Measurement of $\tau_\mu$ . . . . .	67
<b>Conclusion</b> . . . . .	<b>69</b>
<b>References</b> . . . . .	<b>71</b>

# List of Figures

1	Illustration of a thought experiment: Two observers witness the same event with different elapsed times, due to the relative motion between their reference frames. . . . .	3
1.1	A muon at rest decays into an electron, a muon neutrino, and an electron antineutrino. . . . .	5
1.2	The fundamental vertex for the charged-current interaction. . . . .	6
1.3	Some examples of charged weak interactions: (a) A muon absorbs a $W^+$ boson to produce a muon neutrino. (b) A $W^-$ boson produces an electron and an electron antineutrino. (c) An anti-tau interacts with a tau neutrino to produce a $W^+$ boson. . . . .	6
1.4	The principal (most probable) decay mode of the muon, $\mu^- \rightarrow e^- + \nu_\mu + \bar{\nu}_e$ . . . . .	7
1.5	A generic Feynman diagram depicting incoming particles with four-momenta $p_1, p_2$ , interacting to produce the final state of particles with four-momenta, $p_3, p_4$ . . . . .	17
1.6	A marked-up Feynman diagram of the lowest order muon decay, showing internal and external momenta. . . . .	20
1.7	Spectrum of $e^\pm$ energy in $\mu^\pm$ decays, as predicted by the lowest-order Feynman diagram (dotted) and with first-order radiative corrections (solid). Energies are normalized to $E_{max}$ . . . . .	26
2.1	A particle incident in area $d\sigma$ is scattered into solid angle $d\Omega$ . . . . .	27
2.2	The electric field of a moving point charge is distorted by the Lorentz transformation. . . . .	31
2.3	The collisional, radiative, and total stopping power of electrons and positrons in polyvinyltoluene-based scintillator, calculated from the NIST EStar database. . . . .	35
2.4	Probability density functions modeling energy loss fluctuations in thick (left) and thin (right) absorbers. On the left, the number of large-energy-transfer collisions is small compared to the total number of collisions; the <i>pdf</i> is approximately Gaussian. On the right, large-energy-transfer collisions skew the <i>pdf</i> such that the mean and most probable energy loss no longer coincide: $\Delta_p \neq \langle \Delta \rangle$ . . . . .	36

2.5	Energy level diagram of excitation and luminescence processes in an organic molecule with $\pi$ -electronic structure. (From H. Xu, R. Chen, Q. Sun, W. Lai, Q. Su, W. Huang, and X. Liu, <i>Recent progress in metal-organic complexes for optoelectronic applications</i> , Chem. Soc. Rev. 2014, 43, 3259-3302. Published online 2/17/2014, Creative Commons License.) . . . . .	37
2.6	The working mechanism of a ternary-solution plastic scintillator, with approximate fluor concentrations (in weight percentage) and energy transfer distances of the sub-processes. (From K.A. Olive <i>et al.</i> (Particle Data Group), Chin. Phys. C, <b>38</b> , 010009 2014) . . . . .	39
2.7	The composite light yield of a scintillator, represented by the sum of two exponential decays– the prompt and delayed components. . . . .	40
2.8	Basic elements of a photomultiplier tube. . . . .	41
2.9	Left: Probability distributions of secondary electron emission at the first dynode of a PMT, due to 1,2,3, and 4 incident photoelectrons. Statistical broadening of $P(N)$ increases as the number of photoelectrons increases. Right: Low-end of a simulated pulse height spectrum of a PMT. At low pulse heights, the dependence on the first dynode's $\delta$ results in distinguishable peaks corresponding to 1, 2, and 3 photo-electron events. . . . .	44
3.1	Compensating the light collection for near-PMT events by a reflective shield. . . . .	46
3.2	The PMT's dynode output signal for two events: (a) A muon passing straight through the detector, and (b) A muon enters with low energy, is brought to rest, and decays to produce an electron, which generates a second pulse. . . . .	47
3.3	The energy spectra of $e^\pm$ emitted in muon decay, in an ‘ideal’ scintillator with infinite volume (left) and the ‘real’ scintillator with finite volume (right). The effect of electron-escape obscures the underlying distribution of energy, $P(e^\pm)$ . . . . .	48
3.4	Global and local coordinate conventions in the Monte Carlo transport program. . . . .	50
3.5	A particle with initial trajectory $w$ is scattered at the origin by some angle $\theta_s$ , and rotated by $\phi_s$ . The new trajectory, $\{\theta', \phi'\}$ , is determined by calculating the polar angle between $Z$ and $\alpha$ , and the azimuthal angle between $X$ and the projection of $\alpha$ into the $X - Y$ plane. . . . .	51
3.6	Mean free paths for the production of $\delta$ -rays with $T > T_{cut}$ by $e^\pm$ with total energies from 2.011 - 50 MeV (positrons) and from 3.511-50 MeV (electrons). By imposing the limit $T_{cut} = 1.5$ MeV, the mean free path is of the same length scale as the detector, and so the number of $\delta$ -rays produced will not be too large. . . . .	52
3.7	A particle of kinetic energy $E_k$ and mass $m$ transfers kinetic energy $T$ to a particle with the same mass initially at rest. After collision, the incident particle is scattered by $\theta_s$ , and the target particle is scattered by $\theta_r$ . . . . .	54

3.8	Plot of Vavilov's $\kappa$ parameter for $e^\pm$ traveling in PVT-based scintillator. Because $\kappa < 10$ for energies in the range .511 – 55 MeV, we use the Landau-Vavilov most probable energy loss, rather than the Bethe-Bloch mean energy loss. . . . .	55
3.9	Simulated particle tracks for 20 electrons with the same initial configuration, starting from the red dot at $\{0, 39\}$ with trajectory $\{\pi, 0\}$ and total energy 50.511 MeV. Primary electron paths are colored in black, while $\delta$ -ray paths are colored in blue. For this simulation, $E_{cut} = .5$ MeV, $T_{cut} = 1.5$ MeV, and $s = .2$ cm. Every simulated particle deposited its available 50 MeV within the detector. . . . .	58
4.1	Experimental distributions of normalized $e^\pm$ energy, $\chi$ . There are 4291 events in the set collected with the PMT operating at 1200V, and 3286 events from the set collected at 1000V. Both distributions have 30 bins. . . . .	61
4.2	Renormalized distribution of the 1500 lowest-energy events from the 1200V-data, in 15 bins (black) and with an interpolation of the distribution overlaid (red). We can distinguish the characteristic peaks of 1,2, and 3-photoelectron events, for which the statistical broadening of $\delta$ at the first dynode is small, as described in Chapter 2. . . . .	62
4.3	Sum of squared residuals between the $m_\mu = 105$ simulated distribution and the experimental distribution with increasing cuts to the high-energy range (Left), and plots of the closest agreement between experimental and simulated distributions, when $n_{cuts} = 11$ (Right). The experimental distribution is plotted in Black, and the simulated distribution is plotted in Cyan. The simulated distribution is generated from 100000 events, and normalized to the size of the experimental distribution after high-range cuts. . . . .	65
4.4	Left: Experimental distribution of normalized energy $\chi$ from 1200V-data (Black) plotted with simulated distributions assuming different values for $m_\mu$ (Color). Right: The sum of squared residuals between the experimental distribution and simulated distributions at different values of $m_\mu$ . We see that $m_\mu = 105$ MeV produces the strongest agreement (minimum residuals) between observed and simulated results, in agreement with the known value $m_\mu = 105.6583715 \pm 0.0000035$ MeV[21]. . . . .	66
4.5	Left: Experimental energy distribution from 1000V-data (Black) plotted with simulated distributions at different values of $m_\mu$ (Color). The vertical dotted line represents the threshold $\chi$ , above which we calculate the residuals. Right: The sum of squared residuals over the 9 highest bins between experimental and simulated distributions. $m_\mu = 105$ MeV produces the strongest agreement between observed and simulated results, and supports the same finding from the 1200V-data. . . . .	67
4.6	Histogram of decay times $\Delta t$ separating candidate signals of two-pulse events in the 1000V-data. Fitting this histogram to an exponential function (Red) gives us that the observed muon lifetime is $\tau_\mu \approx 2.193 \times 10^{-6}$ s. . . . .	68



# Abstract

An experiment to measure the muon's mass is described. An NI LabVIEW program, together with a digitizing oscilloscope, detect the decay of cosmic ray muons into electrons (or positrons) within a large volume scintillation detector. The energies of the decay products are quantified by integrating the area under the signals produced by the PMT. The mass of the muon is measured by a least-squares-comparison with Monte Carlo generated distributions assuming different values for  $m_\mu$ , with energy deposition modeled by a mixed-class simulation. It is found that a value of  $m_\mu = 105$  MeV most closely matches the experimental distribution.



# Introduction

## Origins

On August 7, 1912, Victor Hess and two colleagues carried three electrometers in a free-balloon flight to an altitude of 5300 meters[1] and found that the ionization rate increased nearly fourfold over that at sea level, suggesting a powerful radiation source was at all times striking the atmosphere from space. Hess and his colleagues ruled out the Sun as a potential radiation source by repeating the balloon ascents over several days and nights, and once even during a solar eclipse. In his words, “*The results of my observation are best explained by the assumption that a radiation of very great penetrating power enters our atmosphere from above.*” For their meticulous efforts, Victor Hess and colleague Carl Anderson received the Nobel Prize in Physics in 1936.

This radiation was first thought to be high-energy photons or *rays*, until it was discovered that their intensity varied with latitude, indicating that they were deflected by Earth’s magnetic field and therefore were charged particles, not photons. Indeed, almost 79% of cosmic rays reaching the top of Earth’s atmosphere are protons, 15% are helium nuclei, and the remainder are mostly electrons or heavier nuclei such as carbon, oxygen, and iron that are synthesized in stars[2].

Cosmic rays travel to us over tremendous interstellar distances, accelerated to near the speed of light by electric fields in space. Earth’s atmosphere is constantly bombarded by these high-energy cosmic rays, the most energetic of which have 40 million times the energy of particles produced at the Large Hadron Collider. On reaching the upper atmosphere, they collide with air molecules to produce fantastic cascades of secondary particles called ‘air showers’.

The particles in these air showers continue to travel towards the Earth’s surface, decaying into lighter and lighter generations of matter. At sea level, the majority of particles to reach us are muons, which are essentially heavier, unstable cousins of the electron. These cosmic muons have long been utilized as a free source of particles for the study of elementary particle physics, astronomy, and atmospheric physics. A popular figure among experimentalists is the rate of muons passing through your opened hand at sea level: approximately 1 per second.

## Cosmic Muons and Time Dilation

The dawn of modern physics in the early 20th century was marked by a series of surprising discoveries that led to significant paradigm shifts. Many would argue that

the advents of quantum mechanics and special relativity are the most important; the term *modern physics* itself is used when either of these theories is incorporated. At its heart, modern physics is the physics of extreme conditions; where quantum mechanics describes the particles that make up our world at low energies and on unbelievably tiny scales, special relativity describes the behavior of space and time at high speeds, comparable to that of light. Picturing physics in these realms, the extremely small and the extremely fast, is often entirely counterintuitive, and there are some surprising predictions to be found therein.

In the year 1905, Albert Einstein revolutionized our view of space and time when he introduced his theory of special relativity. His paper “On the Electrodynamics of Moving Bodies” used two straightforward postulates to derive the laws of special relativity with straightforward trigonometry. The first postulate, attributed to Galileo, is the principle of relativity, which states that the laws of physics are the same in all inertial (non-accelerated) reference frames. A dropped ball falls the same way inside a train-car as it does for someone standing on the ground next to the tracks, except if the train hits a bump or goes into a turn. The second postulate, supported by the null result of the Michelson-Morley experiment, is the constancy of the speed of light; light always travels through a vacuum at a constant speed  $c$ , independent of the motion of the light source *and* the same for all observers.

The invariance of  $c$  in all reference frames has profound consequences, which can be explored by way of thought-experiments. Consider two observers: one sitting inside a bullet train moving at speed  $v$ , the other sitting on the ground to the side of the tracks, as in Figure 1. Within the train car, a source is set up to emit a beam of light, which travels across the car and reflects off a mirror, returning to the source.

In the passenger’s reference frame, the time for the light to bounce back is

$$t_1 = \frac{2d}{c} ,$$

because the light travels the distance  $d$  twice, at speed  $c$ . For the observer on the ground, the time for the same event to occur is of course

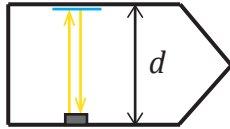
$$t_2 = \frac{2l}{v} ,$$

because the train travels the distance  $l$  twice, moving with speed  $v$ . However, we can also express  $t_2$  in terms of  $c$  by using the Pythagorean theorem:

$$t_2 = \frac{2\sqrt{d^2 + l^2}}{c} .$$

Squaring the above expression and substituting in the previous two expressions,

Passenger's frame:



Observer on the ground:

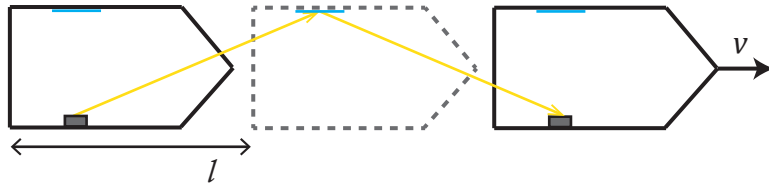


Figure 1: Illustration of a thought experiment: Two observers witness the same event with different elapsed times, due to the relative motion between their reference frames.

rewritten as  $d = ct_1/2$  and  $l = vt_2/2$ , we get

$$\begin{aligned} t_2^2 &= \frac{4}{c^2} \left( \frac{c^2 t_1^2}{4} + \frac{v^2 t_2^2}{4} \right) \\ &= t_1^2 + \frac{v^2}{c^2} t_2^2. \end{aligned}$$

Lastly, by grouping like-terms, we see that

$$t_2 = \frac{t_1}{\sqrt{1 - \frac{v^2}{c^2}}} = \gamma t_1. \quad (1)$$

Astoundingly, the two observers measure a different time interval between the same two events. This phenomenon, known as time dilation<sup>1</sup>, is one of the most important predictions of special relativity. It tells us that there is no preferred or ‘universal’ time frame— contrary to pre-20th century understanding, time and space are not independent, but are inherently linked as a 3+1 dimensional space-time. The ‘Lorentz Factor’,  $\gamma$ , describes the magnitude of the special-relativistic effects between two reference frames, and is always greater than 1.

Time dilation plays a fundamental role in the study of cosmic-ray muons. Muons are unstable particles, decaying after an average lifetime of  $\tau = 2.2 \times 10^{-6}$  s in their rest frame. In an experiment by Frisch and Smith[3], muons were detected atop Mt. Washington in New Hampshire at a rate of 563 per hour, with average speed  $v = .9952 c$ . At this height and speed, the muons would be expected to take  $6.39 \mu s$  to

<sup>1</sup>often memorized by the phrase “fast clocks run slow.”

reach sea level, and therefore should decay before ever reaching the ground. However, another detector at sea level counted 408 muons per hour. The muons are kept from decaying due to the effects of time dilation. Because they travel at .9952  $c$ , their clocks run slow; the fast muon's lifetime is 22.5  $\mu s$  for observers on the ground, and they are able to reach sea level before decaying.

Another special-relativistic effect is implied by this example. If, from the muons perspective, their lifetime is 2.2  $\mu s$ , then they must somehow traverse the distance from mountaintop to sea level before decaying. The answer is that the distance itself is shortened due to the effect of *length contraction*; the actual, physical distance from mountaintop to sea level is shorter in the frame of the fast-traveling muon than for observers on the ground. The effects of time dilation in one frame may be attributed to length contraction as measured in another frame.

## Going Forward

A popular experiment among many universities is to measure the lifetime of the muon using a scintillation detector. In short, this is done by measuring the time interval between two signals; one due to the muon, and one due to the electron produced by its decay. In this thesis, we demonstrate that much of the same equipment may be used to extend the lifetime experiment to the much more sophisticated task of measuring the *mass* of the muon. We do this by measuring the energy of the emitted electron, which is governed by a specific probability distribution.

In Chapter 1, we review Fermi's original theory of muon decay, deriving the probability distribution for electrons to be emitted with specific energies. In Chapter 2, we review the deposition of energy by charged particles traversing matter, as well as the mechanisms of scintillation detectors. In Chapter 3, we discuss the construction and design of the muon detector, and establish the principle of our experiment. In Chapter 4, we present and analyze our data to yield two results, the muon lifetime  $\tau_\mu$  and the muon mass  $m_\mu$ .

# Chapter 1

## Fermi's Theory of Muon Decay

The principal experimental observables in particle physics are the scattering cross section  $\sigma$ , which represents the probability of an incident particle to be scattered from its target, and the decay width  $\Gamma$ , which represents the probability per unit time that a given particle will decay. Our goal in this chapter is to develop an understanding of the muon's decay process as depicted in Figure 1.1.

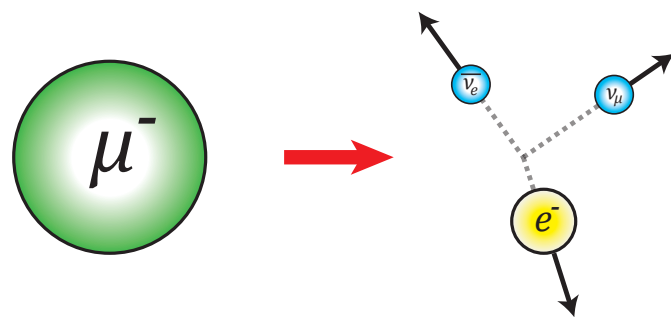


Figure 1.1: A muon at rest decays into an electron, a muon neutrino, and an electron antineutrino.

### Feynman Diagrams

In the Standard Model, particles interact with one another by the exchange of other force-carrying or ‘mediating’ particles. The four known fundamental forces of nature are the strong, electromagnetic, weak, and gravitational forces, and to each force there belongs a physical theory and hypothetically, a mediating particle.

Feynman diagrams graphically represent the interactions of particles as arrangements of ‘fundamental vertices’, at which a force-carrying particle couples to an el-

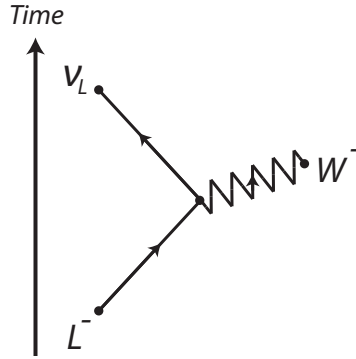


Figure 1.2: The fundamental vertex for the charged-current interaction.

ementary particle. In Figure 1.2, the fundamental vertex of the charged weak interaction shows a charged lepton  $L^-$  converting into a neutrino of the same flavor,  $\nu_L$ , by the emission of a  $W^-$  boson<sup>1</sup>. Evidently, both charge and lepton number are conserved at this vertex.

In Feynman diagrams, time runs along the vertical axis; the diagrams contain no actual ‘spatial’ information about the interacting particles, despite their graphical nature. For this reason, the components in a Feynman diagram can be flipped and rotated into any configuration we like, so long as each vertex is a fundamental vertex. With this in mind, a particle arrow running backwards in time is interpreted as the corresponding antiparticle moving forwards in time. Figure 1.3 shows some of the allowed transformations of the charged weak fundamental vertex.

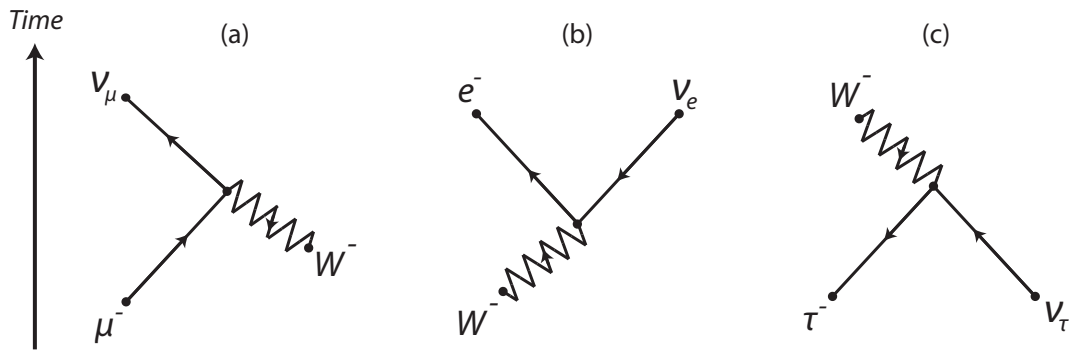


Figure 1.3: Some examples of charged weak interactions: (a) A muon absorbs a  $W^+$  boson to produce a muon neutrino. (b) A  $W^-$  boson produces an electron and an electron antineutrino. (c) An anti-tau interacts with a tau neutrino to produce a  $W^+$  boson.

---

<sup>1</sup>A mediator of the weak force, the others being  $W^+$  and  $Z$  bosons.

The simplest example of muon decay, with just two vertices, is represented in Figure 1.4. We can just as easily reverse the arrows of the particles in Figure 1.4 to describe the corresponding process for anti-muons:

$$\mu^+ \xrightarrow{W^+} e^+ + \nu_e + \bar{\nu}_\mu . \quad (1.1)$$

Of course, most particles decay by several different routes to give off different products; each route is called a *decay mode*, and each mode has its own decay width. We can also imagine that there are many more-complicated processes by which the decay  $\mu^- \rightarrow e^- + \nu_\mu + \bar{\nu}_e$  could occur, by way of adding ‘intermediate’ vertices between those in Figure 1.4. However, the addition of each vertex reduces the likelihood of that process to occur. As such, the process shown in Figure 1.4 is the most probable decay of the muon *because* it is the simplest one. Nearly 100% of muons will decay by this principal mode[4]; the next most probable mode,  $\mu^- \rightarrow e^- + \nu_\mu + \bar{\nu}_e + e^+ + e^-$ , occurs once every  $\sim 30,000$  decays.

To each Feynman diagram, there is an associated complex number  $\mathcal{M}$  called the *amplitude* of the process, which is calculated by evaluating the diagram according to specific ‘Feynman rules’. These rules come from quantum field theory and will not be derived here, but given as a prescription specific to the weak interaction (see [5]). The amplitudes allow us to calculate decay rates and cross sections, but first, we must review the notation of relativistic kinematics.

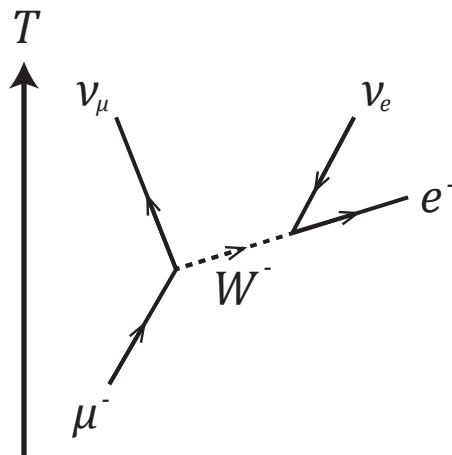


Figure 1.4: The principal (most probable) decay mode of the muon,  $\mu^- \rightarrow e^- + \nu_\mu + \bar{\nu}_e$ .

## 1.1 Relativistic Kinematics

Knowing that time cannot be separated from the three dimensions of space (as in the classical sense), we need new language for describing the behavior of particles in a 3+1 dimensional spacetime. This unification is carried out in the selection of a ‘four-vector’ such that all four coordinates share the same units. By this definition, a point in 4D spacetime is assigned its position-time four-vector  $x^\mu$ , as:

$$x^\mu = (x^0, x^1, x^2, x^3) = (ct, x, y, z) . \quad (1.2)$$

In this notation, a Lorentz transformation between inertial reference frames  $S \rightarrow S'$ , with  $S'$  moving at velocity  $v$  relative to  $S$  along the  $x$ -axis, takes the form of a matrix multiplication as

$$x^{\mu'} = \sum_{\nu=0}^3 \Lambda_\nu^\mu x^\nu \quad \longrightarrow \quad x^{\mu'} = \Lambda_\nu^\mu x^\nu \quad (1.3)$$

where on the right (and from here forward) we adopt Einstein’s summation convention, in which summation is implied over Greek indices that appear twice in one term, one as subscript and one as superscript. The Lorentz transformation is encoded in the coefficients of the matrix  $\Lambda$ ,

$$\Lambda = \begin{bmatrix} \gamma & -\gamma\beta & 0 & 0 \\ -\gamma\beta & \gamma & 0 & 0 \\ 0 & 0 & 1 & 0 \\ 0 & 0 & 0 & 1 \end{bmatrix} \quad (1.4)$$

and any such vector that transforms as  $x^\mu$  in (1.3) is then called a four-vector.

In the same sense that the magnitude of a Euclidean vector pointing from  $a$  to  $b$  in 3D space is invariant to rotations and translations, i.e. the distance between two points is the same for any ‘observer’, the magnitude of a four-vector should be preserved by the Lorentz transformations. To this end, we define the *scalar product* of two four-vectors,  $a^\mu$  and  $b^\mu$ , as

$$a^\mu b_\mu = a^0 b^0 - a^1 b^1 - a^2 b^2 - a^3 b^3 = a_\mu b^\mu \quad (1.5)$$

where *contravariant* four-vectors ( $a^\mu$ ) are ‘index-up’, and *covariant* four-vectors are index-down ( $b_\mu$ ), in keeping consistent with Einstein’s summation convention. The quantity (1.5) is the same number in all inertial reference frames.

The raising and lowering of four-vector indices is accomplished by using the

Minkowski metric  $\eta_{\mu\nu}$ , a second-rank tensor, as

$$a_\mu = \eta_{\mu\nu} a^\nu \quad \text{and} \quad a^\mu = \eta^{\mu\nu} a_\nu , \quad (1.6)$$

where, in the timelike convention<sup>2</sup>,

$$\eta_{\mu\nu} = \begin{bmatrix} 1 & 0 & 0 & 0 \\ 0 & -1 & 0 & 0 \\ 0 & 0 & -1 & 0 \\ 0 & 0 & 0 & -1 \end{bmatrix} = (\eta_{\mu\nu})^{-1} = \eta^{\mu\nu} . \quad (1.7)$$

## Four-Vectors

The position-time four-vector, or simply the ‘four-position’, is but one example of a four-vector. To reiterate, any object with four coordinates that transforms as  $x^\mu$  does in (1.3) is a four-vector. Other properties such as the invariance of the scalar product  $a^\mu b_\mu$  follow from this one condition.

We can express many other useful quantities in four-vector form. To extend our understanding of  $x^\mu$ , consider the notion of *proper time* ( $\tau$ ) as the time elapsed between two events, as measured by an observer passing through those events. Relative to another observer’s time  $t$ , the proper time would be slowed as

$$d\tau = \frac{dt}{\gamma} , \quad (1.8)$$

which is just a restatement of ‘fast clocks run slow’. Importantly, proper time is an invariant quantity, which motivates the idea of a *proper velocity* four-vector (or simply four-velocity):

$$\eta^\mu = \frac{dx^\mu}{d\tau} = \gamma(c, v_x, v_y, v_z) , \quad (1.9)$$

where  $v_x, v_y, v_z$  are just the components of velocity as measured in some observer’s frame.

Naturally, we can then express momentum as a four-vector

$$p^\mu = m_0 \eta^\mu = \left( \frac{E}{c}, p_x, p_y, p_z \right) \quad (1.10)$$

where  $E$  refers to the particle’s relativistic energy (in terms of both its relativistic

---

<sup>2</sup>By this, we mean that the four-vector  $a^\mu$  is timelike if  $a^\mu a_\mu > 0$ .

and rest masses,  $m$  and  $m_0$ ),

$$E = mc^2 = (\gamma m_0)c^2 = \frac{m_0 c^2}{\sqrt{1 - v^2/c^2}} . \quad (1.11)$$

The four-vector in (1.10) is the energy-momentum four-vector, or simply the four-momentum.

The invariance of four-vectors is associated with certain physical ideas. Consider the squared length of the four-momentum,

$$\begin{aligned} p_\mu p^\mu &= (m_0)^2 \eta_\mu \eta^\mu \\ &= (m_0)^2 \gamma^2 (c^2 - (v_x^2 + v_y^2 + v_z^2)) \\ &= (m_0)^2 \gamma^2 c^2 (1 - v^2/c^2) \\ &= (m_0 c)^2 \end{aligned} \quad (1.12)$$

which also may be written

$$\begin{aligned} p_\mu p^\mu &= (E^2/c^2) - (p_x^2 + p_y^2 + p_z^2) \\ &= (E^2/c^2) - p^2 . \end{aligned} \quad (1.13)$$

The invariance of the length of the four-momentum, as expressed in (1.12) and (1.13), yields the relativistic energy-momentum relation

$$E^2 = p^2 c^2 + m_0^2 c^4 , \quad (1.14)$$

which relates an object's rest mass  $m_0$  to its total energy  $E$  and momentum  $p$ . That is, the length of  $p^\mu$  is given by  $m_0 c$ . The invariance of this length is associated with the fact that  $m_0$  is the same in all reference frames.

## 1.2 Dirac Particles

The Dirac equation is a relativistic wave equation that describes charged, massive, spin-1/2 particles (such as electrons). It can be derived by ‘factoring’ the relativistic energy-momentum relation,

$$p^\mu p_\mu - (m_0 c)^2 = 0 , \quad (1.15)$$

into the form of:

$$p^\mu p_\mu - (m_0 c)^2 = 0 = (\beta^\kappa p_\kappa + m_0 c)(\gamma^\lambda p_\lambda - m_0 c) . \quad (1.16)$$

Expanding the right-hand expression, we have

$$\beta^\kappa \gamma^\lambda p_\kappa p_\lambda - m_0 c(\beta^\kappa - \gamma^\kappa) p_\kappa - (m_0 c)^2 = 0 , \quad (1.17)$$

where  $\beta^\kappa$  and  $\gamma^\kappa$  are each a set of four coefficients. To eliminate terms linear in  $p_\kappa$ , we must have  $\beta^\kappa = \gamma^\kappa$ , which then requires that

$$\gamma^\kappa \gamma^\lambda p_\kappa p_\lambda - (m_0 c)^2 = 0 . \quad (1.18)$$

To find suitable coefficients  $\gamma^\kappa$  such that

$$p^\mu p_\mu = \gamma^\kappa \gamma^\lambda p_\kappa p_\lambda = (\gamma^\kappa p_\kappa)(\gamma^\lambda p_\lambda) \quad (1.19)$$

requires that the elements of  $\gamma$  be *matrices*, and not coefficients. That is, we must not only have  $(\gamma^0)^2 = 1$  and  $(\gamma^i)^2 = -1$  for  $i = 1, 2, 3$ , but also that  $\gamma^\kappa \gamma^\lambda + \gamma^\lambda \gamma^\kappa = 0$  for  $\kappa \neq \lambda$ , i.e., the cross-terms arising from the multiplication on the right-hand side of (1.19) should vanish. One set of matrices satisfying these conditions are:

$$\gamma^0 = \begin{pmatrix} 1 & 0 \\ 0 & -1 \end{pmatrix}, \quad \gamma^i = \begin{pmatrix} 0 & \sigma^i \\ -\sigma^i & 0 \end{pmatrix} \quad (1.20)$$

where 1 denotes the  $2 \times 2$  identity matrix, 0 is an empty  $2 \times 2$  matrix, and  $\sigma^i$  ( $i = 1, 2, 3$ ) are the Pauli matrices:

$$\sigma^1 = \begin{pmatrix} 0 & 1 \\ 1 & 0 \end{pmatrix}, \quad \sigma^2 = \begin{pmatrix} 0 & -i \\ i & 0 \end{pmatrix}, \quad \sigma^3 = \begin{pmatrix} 1 & 0 \\ 0 & -1 \end{pmatrix} . \quad (1.21)$$

By reformulating the relativistic energy-momentum relation to the form of (1.16), now a  $4 \times 4$  matrix equation, we get the Dirac equation by setting one of the right-hand factors to zero and applying the quantum substitution  $p_\mu \rightarrow i\hbar \partial_\mu$ :

$$(\gamma^\mu p_\mu - m_0 c) = 0 \quad \rightarrow \quad i\hbar \gamma^\mu \frac{\partial}{\partial x^\mu} \psi - m_0 c \psi = 0 \quad (1.22)$$

Here,  $\psi$  is now a four-element column matrix called a ‘Dirac spinor’. For compatibility with the  $\gamma^\mu$  matrix notation, we sometimes refer to  $\psi$  as a ‘bispinor’ of two components

$\psi_A$  and  $\psi_B$ , which themselves each have two components:

$$\psi = \begin{pmatrix} \psi_A \\ \psi_B \end{pmatrix} = \begin{bmatrix} \psi_1 \\ \psi_2 \\ \psi_3 \\ \psi_4 \end{bmatrix} . \quad (1.23)$$

## Zero-Momentum Solutions

A particle at rest has an infinitely large de Broglie wavelength and a spatially uniform wave function ( $p_\mu\psi = i\hbar\partial_\mu\psi = 0$  for  $\mu = 1, 2, 3$ ). The Dirac equation (1.22) then reduces to its first component,

$$i\hbar\gamma^0 \frac{1}{c} \frac{\partial}{\partial t} \psi - m_0 c \psi = 0 , \quad (1.24)$$

or more clearly,

$$\begin{bmatrix} 1 & 0 & 0 & 0 \\ 0 & 1 & 0 & 0 \\ 0 & 0 & -1 & 0 \\ 0 & 0 & 0 & -1 \end{bmatrix} \frac{\partial\psi}{\partial t} = -\frac{im_0c^2}{\hbar}\psi , \quad (1.25)$$

for which the solutions are:

$$\begin{aligned} \psi^{(1)} &= e^{-(im_0c^2/\hbar)t} \begin{bmatrix} 1 \\ 0 \\ 0 \\ 0 \end{bmatrix} , \quad \psi^{(2)} = e^{-(im_0c^2/\hbar)t} \begin{bmatrix} 0 \\ 1 \\ 0 \\ 0 \end{bmatrix} , \\ \psi^{(3)} &= e^{+(im_0c^2/\hbar)t} \begin{bmatrix} 0 \\ 0 \\ 1 \\ 0 \end{bmatrix} , \quad \psi^{(4)} = e^{+(im_0c^2/\hbar)t} \begin{bmatrix} 0 \\ 0 \\ 0 \\ 1 \end{bmatrix} . \end{aligned} \quad (1.26)$$

From the characteristic time dependence of a quantum state,  $e^{-iEt/\hbar}$ , we see that  $\psi^{(1)}$  and  $\psi^{(2)}$  are positive-energy solutions, describing spin-up and spin-down electrons, respectively. The  $\psi^{(3)}$  and  $\psi^{(4)}$  are negative-energy solutions, which we take to represent antiparticles with *positive* energy. They describe spin-down and spin-up positrons, respectively.

## Free Motion of a Dirac Particle

We want to find plane-wave solutions to the Dirac equation, corresponding to free particles of definite momentum, of the form

$$\psi(x^\mu) = e^{-ik_\mu x^\mu} u(k^\mu) , \quad (1.27)$$

for some four-vector  $k^\mu$  and associated bispinor  $u(k^\mu)$ . Noting that

$$\frac{\partial}{\partial x^\mu} \psi(x^\mu) = -ik_\mu \psi(x^\mu) , \quad (1.28)$$

the Dirac equation then reads

$$i\hbar \gamma^\mu (-ik_\mu \psi(x^\mu)) - m_0 c \psi(x^\mu) = 0 , \quad (1.29)$$

or more simply,

$$(\hbar \gamma^\mu k_\mu - m_0 c) u(k^\mu) = 0 . \quad (1.30)$$

It is then sufficient that  $u(k^\mu)$  satisfy (1.30) to ensure that  $\psi(x^\mu)$  satisfies the Dirac equation. With the  $\gamma^\mu$  matrices written in the Pauli convention (1.20), we have

$$\begin{aligned} \gamma^\mu k_\mu &= \gamma^0 k^0 - \gamma^1 k^1 - \gamma^2 k^2 - \gamma^3 k^3 \\ &= \gamma^0 k^0 - \boldsymbol{\gamma} \cdot \mathbf{k} \\ &= \begin{pmatrix} k^0 & -\mathbf{k} \cdot \boldsymbol{\sigma} \\ \mathbf{k} \cdot \boldsymbol{\sigma} & -k^0 \end{pmatrix} \end{aligned} \quad (1.31)$$

with  $\mathbf{k} = (k^1, k^2, k^3)$  and  $\boldsymbol{\sigma} = (\sigma^1, \sigma^2, \sigma^3)$ . Expressing  $u(k^\mu)$  as a bispinor of  $u_A$  and  $u_B$ , then the condition (1.30) reads

$$(\hbar \gamma^\mu k_\mu - m_0 c) \begin{pmatrix} u_A \\ u_B \end{pmatrix} = \begin{pmatrix} (\hbar k^0 - m_0 c) u_A - \hbar (\mathbf{k} \cdot \boldsymbol{\sigma}) u_B \\ \hbar (\mathbf{k} \cdot \boldsymbol{\sigma}) u_A - (\hbar k^0 + m_0 c) u_B \end{pmatrix} , \quad (1.32)$$

which must equal zero, requiring that

$$u_A = \frac{\mathbf{k} \cdot \boldsymbol{\sigma}}{k^0 - m_0 c / \hbar} u_B \quad \text{and} \quad u_B = \frac{\mathbf{k} \cdot \boldsymbol{\sigma}}{k^0 + m_0 c / \hbar} u_A . \quad (1.33)$$

We substitute  $u_B$  into  $u_A$  to solve the simultaneous equations, which gives us

$$u_A = \frac{(\mathbf{k} \cdot \boldsymbol{\sigma})^2}{(k^0)^2 - (m_0 c/\hbar)^2} u_A . \quad (1.34)$$

Noting that

$$\mathbf{k} \cdot \boldsymbol{\sigma} = \begin{pmatrix} k^3 & k^1 - ik^2 \\ k^1 + ik^2 & -k^3 \end{pmatrix}, \quad (1.35)$$

and consequently

$$(\mathbf{k} \cdot \boldsymbol{\sigma})^2 = \mathbf{k}^2 \begin{pmatrix} 1 & 0 \\ 0 & 1 \end{pmatrix}, \quad (1.36)$$

we see that

$$\mathbf{k}^2 = (k_0)^2 - (m_0 c/\hbar)^2 \quad \rightarrow \quad \left( \frac{m_0 c}{\hbar} \right)^2 = k_\mu k^\mu . \quad (1.37)$$

This tells us that our plane-wave solution satisfies the Dirac equation so long as  $k^\mu$  is associated with the particle and has a squared length of  $(m_0 c/\hbar)^2$ . The energy-momentum four-vector meets these requirements,

$$k^\mu = \pm \frac{p^\mu}{\hbar}, \quad (1.38)$$

where we choose  $p^\mu$  to be positive for particle states and negative for antiparticle states, providing the desired time dependence of  $e^{\mp iEt/\hbar}$ . Free-particle solutions are constructed by picking

$$\begin{aligned} u_A &= N\chi \\ u_B &= N\chi', \end{aligned} \quad (1.39)$$

where  $\chi$  and  $\chi'$  are two-component spinors and  $N$  is a normalization constant. There exist four linearly independent bispinors  $u(k^\mu) = (u_A, u_B)^T$  which correspond to the two linearly-independent choices of each of  $\chi$  and  $\chi'$ . That is, we pick  $\chi_r$  and  $\chi'_r$ , where  $r = 1, 2$ , as

$$\chi_1 = \chi'_1 = \begin{pmatrix} 1 \\ 0 \end{pmatrix} \quad \text{and} \quad \chi_2 = \chi'_2 = \begin{pmatrix} 0 \\ 1 \end{pmatrix}, \quad (1.40)$$

and for each choice of either  $u_A$  or  $u_B$ , we construct the other using our conditions

on  $u(k^\mu)$  from (1.33). This process yields two particle solutions

$$\begin{aligned} u_A^1 &= \begin{pmatrix} 1 \\ 0 \end{pmatrix} \quad \rightarrow \quad u_B^1 = \frac{c}{E + m_0 c^2} \begin{pmatrix} p_z \\ p_+ \end{pmatrix}, \\ u_A^2 &= \begin{pmatrix} 0 \\ 1 \end{pmatrix} \quad \rightarrow \quad u_B^2 = \frac{c}{E + m_0 c^2} \begin{pmatrix} p_- \\ -p_z \end{pmatrix}, \end{aligned} \quad (1.41)$$

for which  $k^\mu$  must be positive so that  $u_B$  is defined in the limit as  $\mathbf{p} \rightarrow 0$ . Likewise, we have two antiparticle solutions with  $k^\mu$  negative,

$$\begin{aligned} u_B^3 &= \begin{pmatrix} 1 \\ 0 \end{pmatrix} \quad \rightarrow \quad u_A^3 = \frac{c}{E + m_0 c^2} \begin{pmatrix} p_z \\ p_+ \end{pmatrix}, \\ u_B^4 &= \begin{pmatrix} 0 \\ 1 \end{pmatrix} \quad \rightarrow \quad u_A^4 = \frac{c}{E + m_0 c^2} \begin{pmatrix} p_- \\ -p_z \end{pmatrix}, \end{aligned} \quad (1.42)$$

where  $p_\pm$  represents the complex form  $p_x \pm i p_y$ . It is customary to represent the particle solutions by  $u^{(1)} = (u_A^1, u_B^1)^T$  and  $u^{(2)} = (u_A^2, u_B^2)^T$ , whereas the antiparticle solutions are  $v^{(1)} = (u_A^3, u_B^3)^T$  and  $v^{(2)} = -(u_A^4, u_B^4)^T$ . The adjoint of a bispinor is defined as  $\bar{u} = u^\dagger \gamma^0$ ,  $\bar{v} = v^\dagger \gamma^0$ , where  $\dagger$  signifies the Hermitian conjugate.

By convention, we choose the normalization condition

$$u(k^\mu)^\dagger u(k^\mu) = 2 \frac{E}{c}, \quad (1.43)$$

And the normalization factor is then

$$N = \sqrt{\frac{E + m_0 c^2}{c}}. \quad (1.44)$$

The free-particle bispinors have the important properties of being orthogonal,

$$\bar{u}^{(1)} u^{(2)} = 0, \quad \bar{v}^{(1)} v^{(2)} = 0, \quad (1.45)$$

and complete,

$$\sum_{s=1,2} u^{(s)} \bar{u}^{(s)} = (\gamma^\mu p_\mu + m_0 c), \quad \sum_{s=1,2} v^{(s)} \bar{v}^{(s)} = (\gamma^\mu p_\mu - m_0 c). \quad (1.46)$$

The canonical free-particle solutions are then:

$$\begin{aligned}
\psi^{(1)}(x^\mu) &= e^{-ip_\mu x^\mu/\hbar} u^{(1)}(k^\mu) = \sqrt{\frac{E + m_0 c^2}{c}} \begin{pmatrix} 1 \\ 0 \\ \frac{c(p_z)}{E+m_0 c^2} \\ \frac{c(p_+)}{E+m_0 c^2} \end{pmatrix} e^{-ip_\mu x^\mu/\hbar}, \\
\psi^{(2)}(x^\mu) &= e^{-ip_\mu x^\mu/\hbar} u^{(2)}(k^\mu) = \sqrt{\frac{E + m_0 c^2}{c}} \begin{pmatrix} 0 \\ 1 \\ \frac{c(p_-)}{E+m_0 c^2} \\ \frac{c(-p_z)}{E+m_0 c^2} \end{pmatrix} e^{-ip_\mu x^\mu/\hbar}, \\
\psi^{(3)}(x^\mu) &= e^{ip_\mu x^\mu/\hbar} v^{(1)}(k^\mu) = \sqrt{\frac{E + m_0 c^2}{c}} \begin{pmatrix} \frac{c(p_-)}{E+m_0 c^2} \\ \frac{c(-p_z)}{E+m_0 c^2} \\ 0 \\ 1 \end{pmatrix} e^{ip_\mu x^\mu/\hbar}, \\
\psi^{(4)}(x^\mu) &= e^{ip_\mu x^\mu/\hbar} v^{(2)}(k^\mu) = -\sqrt{\frac{E + m_0 c^2}{c}} \begin{pmatrix} \frac{c(p_z)}{E+m_0 c^2} \\ \frac{c(p_+)}{E+m_0 c^2} \\ 1 \\ 0 \end{pmatrix} e^{ip_\mu x^\mu/\hbar}.
\end{aligned} \tag{1.47}$$

### 1.3 The Feynman Calculus for Weak Interactions

We want to apply our knowledge of Dirac particles to the calculation of cross sections and decay widths. These calculations are done using Fermi's ‘Golden Rule’, which states that the transition rate from one energy eigenstate to another due to a perturbation is

$$\Gamma_{i \rightarrow f} = \frac{2\pi}{\hbar} |\langle f | H' | i \rangle|^2 \rho, \tag{1.48}$$

where the kinematical factor  $\rho$  is the density of final states, and  $\langle f | H' | i \rangle$  is the matrix element of the perturbation Hamiltonian  $H'$  between the initial and final states. This equation is nonrelativistic, but its implications are worth considering in order to better understand quantum transitions.

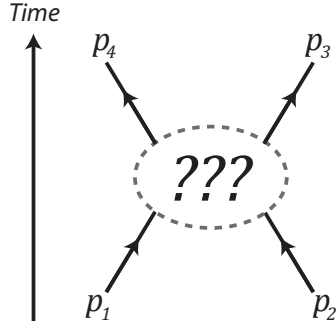


Figure 1.5: A generic Feynman diagram depicting incoming particles with four-momenta  $p_1, p_2$ , interacting to produce the final state of particles with four-momenta,  $p_3, p_4$ .

Conceptually, Fermi's Golden Rule states the transition rate for a process depends separately on two factors: the amplitude  $\mathcal{M} = \langle f | H' | i \rangle$ , and the phase space  $\rho$ . The amplitude contains all of the dynamical information of a given process, describing the strength of the coupling between  $|i\rangle$  and  $|f\rangle$  states. The density of final states,  $\rho$ , describes the number of ways the transition can occur, i.e., the ways of distributing the total four-momentum over all outgoing particles, subject to some kinematic constraints.

As a mathematical tool, a Feynman diagram of amplitude  $\mathcal{M}$  represents a perturbative contribution to the total amplitude of the quantum transition  $|i\rangle \rightarrow |f\rangle$ . By  $|i\rangle$  and  $|f\rangle$ , we mean the outermost lines corresponding to the initial and final particles of an interaction, as in Figure 1.5. The interior dynamics are virtual, in that they represent the different ways  $|i\rangle \rightarrow |f\rangle$  could occur. In theory, we would need to sum the amplitudes of all Feynman diagrams that depict  $|i\rangle \rightarrow |f\rangle$ , of which there are infinitely many, to get the exact transition amplitude. However, each vertex introduces a factor of  $\alpha_w = 10^{-6}$  such that we can limit our focus to diagrams of lowest order.

Supposing a particle 1 decays into any number of other particles  $2, 3, \dots, n$ , then the relativistic Golden Rule for the decay rate is given by

$$\Gamma = \frac{S}{2\hbar m_1} \int |\mathcal{M}|^2 (2\pi)^4 \delta^4(p_1 - p_2 - \dots - p_n) \times \prod_{j=2}^n 2\pi \delta(p_j^2 - m_j^2 c^2) \theta(p_j^0) \frac{d^4 p_j}{(2\pi)^4}, \quad (1.49)$$

where  $m_i$  is the rest mass of the  $i$ th particle,  $p_i$  is its four-momentum, and  $\theta(p_j^0)$  is

the Heaviside step-function. The  $S$  factor corrects for double-counting of identical particles in the final state:

$$S = \prod_{i=1}^N \frac{1}{s_i!} \quad (1.50)$$

where  $s_i$  is the number of particles of species  $i$ , in a process that produces  $N$  distinct particle species.

The Feynman rules tell us how to construct  $\mathcal{M}$  for a given Feynman diagram. These can be derived from the Lagrangian density in quantum field theory, but here, will simply be given as prescription. The process is:

1. Assign a momentum  $p_i$  to each external line, and  $q_i$  to each internal line. Draw an arrow next to every line, running forward in time.
2. Incoming external lines contribute a factor of  $u$  or  $\bar{v}$  for leptons and antileptons, respectively. Outgoing external lines contribute  $\bar{u}$  or  $v$ , again for leptons and antileptons.
3. Each vertex contributes a factor of

$$\frac{-ig_w}{2\sqrt{2}} \gamma^\mu (1 - \gamma^5) \quad (1.51)$$

for weak coupling constant<sup>3</sup>  $g_w = \sqrt{4\pi\alpha_w}$  and  $\gamma^5 \equiv i\gamma^0\gamma^1\gamma^2\gamma^3 = \begin{pmatrix} 0 & 1 \\ 1 & 0 \end{pmatrix}$ .

4. Each internal line contributes a propagator factor as

$$P(W^\pm) = \frac{-i(\eta_{\mu\nu} - q_\mu q_\nu/M^2c^2)}{q_\mu q^\mu - M^2c^2}$$

for  $W^\pm$  bosons with rest mass  $M$ , and

$$P(L, \bar{L}) = \frac{i(\gamma^\mu q_\mu + m_0 c)}{q_\mu q^\mu - m_0^2 c^2}$$

for leptons or anti-leptons. If  $q_\mu q^\mu \ll (Mc)^2$ , then the propagator of the  $W^\pm$  becomes

$$P(W^\pm) \rightarrow \frac{i\eta_{\mu\nu}}{(M_W c)^2},$$

which, for low energies, is a safe approximation ( $M_W = 80.4 \pm .03 \text{ GeV}/c^2$ ).

---

<sup>3</sup> $g_w \approx .6295$  [5]

5. For each vertex, write a delta function of the form

$$(2\pi)^4 \delta^4(k_1 + k_2 + k_3) ,$$

where the  $k$ 's are the three four-momenta that form the vertex. If an arrow points away from the vertex, then its  $k = -(q_\mu \text{ or } p_\mu)$ .

6. For each internal momentum  $q_i$ , add a factor of

$$\frac{d^4 q_i}{(2\pi)^4}$$

and integrate.

7. Cancel the resulting factor of

$$(2\pi)^4 \delta^4(p_1 + p_2 + \dots + p_n) ,$$

multiply by  $i$ , and the remaining value is  $\mathcal{M}$ .

In practice, it is best to track each particle line backwards through the diagram and write down terms as we encounter them. This procedure ensures that the multiplications of bispinors and matrices are always in correct order, resulting in a single number.

## 1.4 Decay of the Muon

We first apply step 1 to the lowest order Feynman diagram of the muon's decay, as shown in Figure 1.6. We have an incoming lepton with  $p_1$  that contributes a factor of  $u(p_1)$ , two outgoing leptons that contribute  $\bar{u}(p_2)$  and  $\bar{u}(p_4)$ , and one outgoing anti-lepton that contributes a factor of  $v(p_3)$ . Tracing backwards from  $p_2 \rightarrow p_1$ , we get a 'sandwich' of an external line factor, vertex factor, external line factor:

$$\text{Lepton Line Factor } p_2 \rightarrow p_1 = \frac{-ig_w}{2\sqrt{2}} \left[ \bar{u}(p_2) \gamma^\mu (1 - \gamma^5) u(p_1) \right] \quad (1.52)$$

Likewise, we trace backwards from  $p_4 \rightarrow p_3$  to get the term

$$\text{Lepton Line Factor } p_4 \rightarrow p_3 = \frac{-ig_w}{2\sqrt{2}} \left( \frac{i}{(M_W c)^2} \right) \left[ \bar{u}(p_4) \gamma_\mu (1 - \gamma^5) v(p_3) \right] \quad (1.53)$$

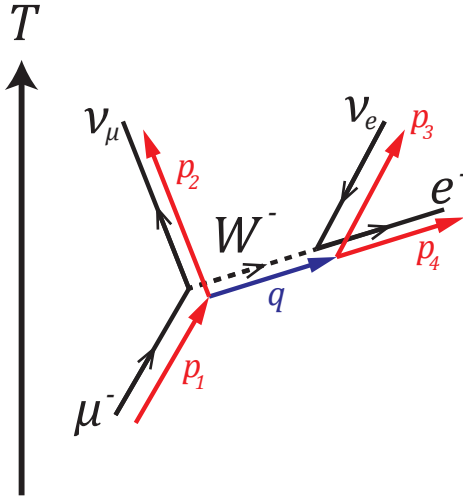


Figure 1.6: A marked-up Feynman diagram of the lowest order muon decay, showing internal and external momenta.

where we have absorbed the  $W$ 's propagator factor, as  $\eta_{\mu\nu}\gamma^\nu \rightarrow \gamma_\mu$ . With just the single internal momentum  $q$ , we apply steps 5-6 to get the momentum-space integrand

$$\begin{aligned} & \frac{-ig_w^2}{8(M_Wc)^2}(2\pi)^4 \int \left[ \bar{u}(p_2)\gamma^\mu(1-\gamma^5)u(p_1) \right] \left[ \bar{u}(p_4)\gamma_\mu(1-\gamma^5)v(p_3) \right] \\ & \quad \times \delta^4(p_1 - p_2 - q) \delta^4(q - p_3 - p_4) d^4q . \end{aligned} \tag{1.54}$$

Conservation of momentum at each vertex is enforced by the delta functions. The trivial  $q$  integration over the second delta function sends  $q \rightarrow p_3 + p_4$ , and we drop the remaining  $(2\pi)^4\delta^4(p_1 - p_2 - p_3 - p_4)$  factor, as in step 7. Multiplying by  $i$ , then, we have

$$\mathcal{M} = \frac{g_w^2}{8(M_Wc)^2} \left[ \bar{u}(p_2)\gamma^\mu(1-\gamma^5)u(p_1) \right] \left[ \bar{u}(p_4)\gamma_\mu(1-\gamma^5)v(p_3) \right] . \tag{1.55}$$

We are left with a term in bispinors  $u, \bar{u}, v$ , which in theory could be specified given some initial and final spin configurations to calculate the amplitude  $\mathcal{M}_{s_i \rightarrow s_f}$ . For our purposes, we are instead interested in the amplitude that represents the average over all initial spin configurations, and the sum over all final spin configurations,  $\langle |\mathcal{M}|^2 \rangle$ . Such an average is appropriate because we never directly observe the spin states of the muon or the electron.

## Casimir's Trick

Squaring the amplitude, we have

$$\begin{aligned} |\mathcal{M}|^2 &= \left( \frac{g_w^2}{8(M_W c)^2} \right)^2 \left[ \bar{u}(p_2) \gamma^\mu (1 - \gamma^5) u(p_1) \right] \left[ \bar{u}(p_4) \gamma_\mu (1 - \gamma^5) v(p_3) \right] \\ &\quad \times \left[ \bar{u}(p_2) \gamma^\nu (1 - \gamma^5) u(p_1) \right]^* \left[ \bar{u}(p_4) \gamma_\nu (1 - \gamma^5) v(p_3) \right]^*, \end{aligned} \quad (1.56)$$

which is expressed as two factors of the form

$$\begin{aligned} G_1 &\equiv \left[ \bar{u}(p_2) \Gamma_1 u(p_1) \right]^* \left[ \bar{u}(p_2) \Gamma_2 u(p_1) \right]^*, \\ G_2 &\equiv \left[ \bar{u}(p_4) \Gamma_3 v(p_3) \right]^* \left[ \bar{u}(p_4) \Gamma_4 v(p_3) \right]^*. \end{aligned} \quad (1.57)$$

We note that

$$\begin{aligned} \left[ \bar{u}(p_2) \Gamma_2 u(p_1) \right]^* &= u^\dagger(p_1) \Gamma_2^\dagger \gamma^{0\dagger} u(p_2) \\ \text{and} \\ \left[ \bar{u}(p_4) \Gamma_4 v(p_3) \right]^* &= v^\dagger(p_3) \Gamma_4^\dagger \gamma^{0\dagger} u(p_4), \end{aligned} \quad (1.58)$$

and, inserting  $(\gamma^0)^2 = 1$  before each  $\Gamma$  matrix, we get

$$\begin{aligned} G_1 &= \left[ \bar{u}(p_2) \Gamma_1 u(p_1) \right] \left[ \bar{u}(p_1) \bar{\Gamma}_2 u(p_2) \right] \\ \text{and} \\ G_2 &= \left[ \bar{u}(p_4) \Gamma_3 v(p_3) \right] \left[ \bar{v}(p_3) \bar{\Gamma}_4 u(p_4) \right], \end{aligned} \quad (1.59)$$

where  $\bar{\Gamma}_i \equiv \gamma^0 \Gamma_i^\dagger \gamma^0$ .

We are interested in summing over the spin states for these  $G$  factors. From the completeness of the bispinors, we can combine the bracketed terms as

$$G'_1 = \sum_{p_1 \text{ spins}} G_1 = \bar{u}(p_2) \Gamma_1 (p_1^\mu + m_1 c) \bar{\Gamma}_2 u(p_2) = \bar{u}(p_2) Q^a u(p_2),$$

$$G'_2 = \sum_{p_3 \text{ spins}} G_2 = \bar{u}(p_4) \Gamma_3 (p_3^\mu - m_3 c) \bar{\Gamma}_4 u(p_4) = \bar{u}(p_4) Q^b u(p_4), \quad (1.60)$$

where  $Q^\mu \equiv a^\mu \gamma_\mu$ . If we then sum over  $p_2$  and  $p_4$ 's spin states, we can exploit the

orthogonality of the bispinors to eliminate off-diagonal terms:

$$\begin{aligned} G_1''' &= \sum_{p_2 \text{ spins}} G_1' = \sum_{i,j=1}^4 Q_{ij}^a \left[ \sum_{s=1,2} u^s(p_2) \bar{u}^s(p_2) \right]_{ji} , \\ G_2'' &= \sum_{p_4 \text{ spins}} G_2' = \sum_{i,j=1}^4 Q_{ij}^b \left[ \sum_{s=1,2} u^s(p_4) \bar{u}^s(p_4) \right]_{ji} , \end{aligned} \quad (1.61)$$

and the spin-summed  $G$  factors become the simple equations

$$\begin{aligned} G_1'' &= \text{Tr}[Q^a(p_2 + m_2 c)] , \\ G_2'' &= \text{Tr}[Q^b(p_4 + m_4 c)] . \end{aligned} \quad (1.62)$$

By this process, we have reduced the problem to that of evaluating the trace of a product of matrices. Returning to the amplitude, and assuming the neutrino masses  $m_2$  and  $m_3$  are negligible, we have

$$\begin{aligned} \sum_{\text{spins}} |\mathcal{M}|^2 &= \left( \frac{g_w^2}{8(M_W c)^2} \right)^2 G_1'' G_2'' \\ &= \frac{g_w^4}{8^2(M_W c)^4} \text{Tr}[\Gamma_1(p_1 + m_1 c) \bar{\Gamma}_2(p_2)] \\ &\quad \times \text{Tr}[\Gamma_3(p_3) \bar{\Gamma}_4(p_4 + m_4 c)] \\ &= 4 \left( \frac{g_w}{M_W c} \right)^4 (p_1 \cdot p_3) (p_2 \cdot p_4) . \end{aligned} \quad (1.63)$$

In the last step, we have omitted much of the tedious matrix arithmetic involved in simplifying the trace expressions (see [5] for exposition). We divide by the number of initial spin states, 2, so that we are averaging over initial spins for the muon. Therefore,

$$\langle |\mathcal{M}|^2 \rangle = 2 \left( \frac{g_w}{M_W c} \right)^4 (p_1 \cdot p_3) (p_2 \cdot p_4) . \quad (1.64)$$

In the rest frame of the muon, we have

$$p_1 = (m_\mu c, 0, 0, 0) \quad \longrightarrow \quad (p_1 \cdot p_3) = m_\mu E_3 , \quad (1.65)$$

and also, neglecting neutrino mass ( $p_2^2 = m_\nu^2 c^2 \approx 0$ ),

$$(p_2 + p_4)^2 = (m_e c)^2 + 2(p_2 \cdot p_4) . \quad (1.66)$$

Using conservation of momentum ( $p_1 = p_2 + p_3 + p_4$ ),

$$(p_2 + p_4)^2 = (p_1 - p_3)^2 = (m_\mu c)^2 - 2(p_1 \cdot p_3) , \quad (1.67)$$

and finally we have

$$(p_2 \cdot p_4) = \frac{(m_\mu c)^2 - (m_e c)^2}{2} - m_\mu E_3 . \quad (1.68)$$

The spin-averaged amplitude is

$$\begin{aligned} \langle |\mathcal{M}|^2 \rangle &= \left( \frac{g_w}{M_W c} \right)^4 m_\mu^2 E_3 (m_\mu c^2 - 2E_3) \\ &= \left( \frac{g_w^2 m_\mu}{M_W^2 c} \right)^2 |\mathbf{p}_3| (m_\mu c - 2|\mathbf{p}_3|) , \end{aligned} \quad (1.69)$$

where we have set  $m_e = 0$ . This approximation does not significantly affect the accuracy of our calculation[5]. The decay rate, given by the golden rule, is then

$$d\Gamma = \frac{\langle |\mathcal{M}|^2 \rangle}{2\hbar m_\mu} (2\pi)^4 \delta^4(p_1 - p_2 - p_3 - p_4) \frac{d^3 \mathbf{p}_2}{(2\pi)^3 2|\mathbf{p}_2|} \frac{d^3 \mathbf{p}_3}{(2\pi)^3 2|\mathbf{p}_3|} \frac{d^3 \mathbf{p}_4}{(2\pi)^3 2|\mathbf{p}_4|} , \quad (1.70)$$

and all that is left is to integrate over momentum space. By the decomposition of

$$\delta^4(p_1 - p_2 - p_3 - p_4) = \delta(m_\mu c - |\mathbf{p}_2| - |\mathbf{p}_3| - |\mathbf{p}_4|) \delta^3(\mathbf{p}_2 + \mathbf{p}_3 + \mathbf{p}_4) , \quad (1.71)$$

we integrate over  $\mathbf{p}_2$ , where the  $\delta^3$  function just restricts  $\mathbf{p}_2 \rightarrow -(\mathbf{p}_3 + \mathbf{p}_4)$ , giving us

$$d\Gamma = \frac{\langle |\mathcal{M}|^2 \rangle}{16\hbar m_\mu (2\pi)^5} \delta(m_\mu c - |\mathbf{p}_3 + \mathbf{p}_4| - |\mathbf{p}_3| - |\mathbf{p}_4|) \frac{d^3 \mathbf{p}_3 d^3 \mathbf{p}_4}{|\mathbf{p}_3 + \mathbf{p}_4| |\mathbf{p}_3| |\mathbf{p}_4|} . \quad (1.72)$$

Next, we integrate over  $\mathbf{p}_3$  by fixing the polar axis along  $\mathbf{p}_4$  and transforming to spherical coordinates  $\mathbf{p}_3 = (r, \theta, \phi)$ , where

$$d^3 \mathbf{p}_3 = r^2 \sin \theta dr d\theta d\phi = |\mathbf{p}_3|^2 \sin \theta d|\mathbf{p}_3| d\theta d\phi , \quad (1.73)$$

and defining

$$u^2 \equiv |\mathbf{p}_3 + \mathbf{p}_4|^2 = |\mathbf{p}_3|^2 + |\mathbf{p}_4|^2 + 2|\mathbf{p}_3||\mathbf{p}_4| \cos \theta , \quad (1.74)$$

the integral over  $\phi$  simply adds a factor of  $2\pi$ :

$$d\Gamma = \frac{\langle |\mathcal{M}|^2 \rangle}{16\hbar m_\mu (2\pi)^4} \frac{d^3 \mathbf{p}_4}{|\mathbf{p}_4|} \int \delta(m_\mu c - u - |\mathbf{p}_3| - |\mathbf{p}_4|) \frac{|\mathbf{p}_3| d|\mathbf{p}_3| \sin \theta d\theta}{u} . \quad (1.75)$$

Under the substitution ( $\theta \rightarrow u$ ), we have

$$2u du = -2|\mathbf{p}_3||\mathbf{p}_4| \sin \theta d\theta , \quad (1.76)$$

and therefore, we integrate by

$$d\Gamma = \frac{\langle |\mathcal{M}|^2 \rangle}{16(2\pi)^4 \hbar m_\mu} \frac{d^3 \mathbf{p}_4}{|\mathbf{p}_4|^2} d|\mathbf{p}_3| \int_{u_-}^{u_+} \delta(m_\mu c - u - |\mathbf{p}_3| - |\mathbf{p}_4|) du , \quad (1.77)$$

where

$$u_\pm \equiv \sqrt{|\mathbf{p}_3|^2 + |\mathbf{p}_4|^2 \pm 2|\mathbf{p}_3||\mathbf{p}_4|} = \left| |\mathbf{p}_3| \pm |\mathbf{p}_4| \right| . \quad (1.78)$$

Of course, the integral over  $du$  is 1 if ( $u_- < m_\mu c - |\mathbf{p}_3| - |\mathbf{p}_4| < u_+$ ), and 0 otherwise. This range is equivalent to the restriction that

$$\begin{aligned} |\mathbf{p}_3| &< \frac{m_\mu c}{2} , \\ |\mathbf{p}_4| &< \frac{m_\mu c}{2} , \\ |\mathbf{p}_3| + |\mathbf{p}_4| &> \frac{m_\mu c}{2} , \end{aligned} \quad (1.79)$$

that is, no particle can be emitted with momentum greater than  $m_\mu c/2$ , and conversely, any pair must have combined energy no less than  $m_\mu c/2$ . It is illustrative to consider the particles in the center-of-mass frame; by conservation of momentum, the largest energy any one particle can carry is half of the available energy ( $m_\mu c^2/2$ ), and in this case, the other two particles must be emitted diametrically opposite to the first, such that the total momentum be zero.

By the inequalities in (1.79), we then integrate over  $|\mathbf{p}_3|$  from ( $m_\mu c/2 - |\mathbf{p}_4|$ ) to ( $m_\mu c/2$ ):

$$\begin{aligned} d\Gamma &= \left( \frac{g_w^2}{16\pi^2 M_W^2} \right)^2 \frac{m_\mu}{\hbar c^2} \frac{d^3 \mathbf{p}_4}{|\mathbf{p}_4|^2} \int_{m_\mu c/2 - |\mathbf{p}_4|}^{m_\mu c/2} |\mathbf{p}_3|(m_\mu c - 2|\mathbf{p}_3|) d|\mathbf{p}_3| \\ &= \left( \frac{g_w^2}{16\pi^2 M_W^2} \right)^2 \frac{m_\mu}{\hbar c^2} \left( \frac{m_\mu c}{2} - \frac{2}{3} |\mathbf{p}_4| \right) d^3 \mathbf{p}_4 , \end{aligned} \quad (1.80)$$

and, writing  $d^3 \mathbf{p}_4 = 4\pi |\mathbf{p}_4|^2 d|\mathbf{p}_4|$  in spherical polar form, we get

$$\frac{d\Gamma}{d|\mathbf{p}_4|} = \left( \frac{g_w^2}{16\pi^2 M_W^2} \right)^2 \frac{m_\mu}{\hbar c^2} 4\pi \left( \frac{m_\mu c}{2} |\mathbf{p}_4|^2 - \frac{2}{3} |\mathbf{p}_4|^3 \right) . \quad (1.81)$$

Expressing this in terms of the electron energy  $E = |\mathbf{p}_4|c$ , then

$$\frac{d\Gamma}{dE} = \left(\frac{g_w}{M_W c}\right)^4 \frac{m_\mu^2 E^2}{2\hbar(4\pi)^3} \left(1 - \frac{4E}{3m_\mu c^2}\right), \quad (1.82)$$

which tells us the energy distribution of the electrons emitted in muon decay. Because  $d\Gamma/dE$  is independent of angle, the probability of electrons to be produced with energy  $E_e$  in a given time interval and solid angle is

$$P(E_e) = C(m_\mu c^2 E_e)^2 \left(3 - 4\frac{E_e}{m_\mu c^2}\right), \quad (1.83)$$

for some constant value  $C$ . By integrating (1.82) over energy, the total decay rate is

$$\begin{aligned} \Gamma &= \left(\frac{g_w}{M_W c}\right)^4 \frac{m_\mu^2}{2\hbar(4\pi)^3} \int_0^{m_\mu c^2/2} E^2 \left(1 - \frac{4E}{3m_\mu c^2}\right) dE \\ &= \left(\frac{m_\mu g_w}{M_W}\right)^4 \frac{m_\mu c^2}{12\hbar(8\pi)^3}, \end{aligned} \quad (1.84)$$

and so the lifetime of the muon, to lowest order, is

$$\tau_\mu \equiv \frac{1}{\Gamma} = \left(\frac{M_W}{m_\mu g_w}\right)^4 \frac{12\hbar(8\pi)^3}{m_\mu c^2} \approx 2.532 \mu s. \quad (1.85)$$

The muon decay spectrum and lifetime predicted by this lowest-order Feynman diagram are a close first estimate to the true behavior of muon decay. Ever since its discovery in 1936, the muon has occupied a special role in the field of experimental particle physics. As the only accessible, purely leptonic process, the study of muon decay has been central to understanding weak interactions. Today, its lifetime is known to greater accuracy than any other unstable particle; a wealth of experiments are dedicated to measuring its properties with extremely high precision, in hopes of finding “new physics” beyond the Standard Model[6].

The accuracy of these theoretical predictions is increased by considering the contribution of higher-order processes to the overall amplitude. The next step, beyond the lowest-order diagram, is to factor in radiative corrections arising from the exchange of a virtual photon by the  $\mu^\pm$  and  $e^\pm$ , which add  $\mathcal{O}(\alpha)$  terms. With the addition of first-order radiative corrections, the normalized energy spectrum of electrons and positrons in  $\mu^\pm$  decay is given by[7]

$$P(x) = \frac{G_F^2 m_\mu^5}{96\pi^3} x^2 (3 - 2x) \left\{ 1 + \frac{\alpha}{2\pi} \left( A(x) + \ln \left[ \frac{m_\mu^2}{m_e^2} \right] B(x) \right) \right\}, \quad (1.86)$$

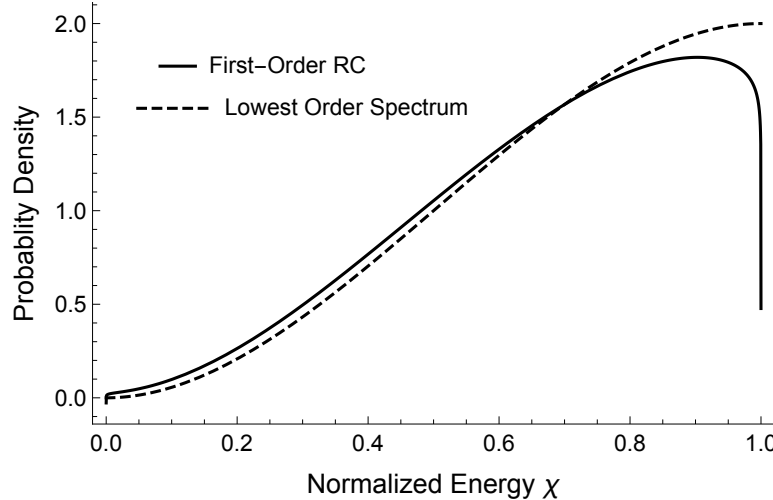


Figure 1.7: Spectrum of  $e^\pm$  energy in  $\mu^\pm$  decays, as predicted by the lowest-order Feynman diagram (dotted) and with first-order radiative corrections (solid). Energies are normalized to  $E_{max}$ .

where  $G_F$  is the Fermi coupling constant and  $x$  is the normalized energy<sup>4</sup> of the  $e^\pm$ , and where

$$\begin{aligned}
 A(x) = & 4\text{Li}_2(x) - \frac{2\pi^2}{3} - 4 + 2\left[3\ln(1-x) - 2\ln x + 1\right]\ln x - 2\frac{1+x}{x}\ln(1-x) \\
 & + \frac{(1-x)(5+17x-16x^2)}{3x^2(3-2x)}\ln x + \frac{(1-x)(-22x+34x^2)}{3x^2(3-2x)}, \\
 B(x) = & 3+4\ln\frac{1-x}{x} + \frac{(1-x)(5+17x-34x^2)}{3x^2(3-2x)}. \tag{1.87}
 \end{aligned}$$

In Figure 1.7, our lowest-order prediction of the  $e^\pm$  energy spectrum from  $\mu^\pm$  decay is compared to the spectrum with first-order radiative corrections. Besides the fact that  $\mathcal{O}(\alpha^2)$  corrections are not well understood for positrons[8], it is clear that higher-order corrections quickly become unwieldy, and are not needed given the simplicity of our detector.

---

<sup>4</sup> $x = E_{e^\pm}/E_{max}$ , where  $E_{max} = (m_\mu^2 + m_e^2)/(2m_\mu)$

# Chapter 2

## The Physics of Scintillation Detectors

Here, we discuss the various components of the scintillation detector: the energy loss of charged particles passing through matter, the production of light in scintillating materials, and the detection of these light pulses by photomultiplier tubes.

### 2.1 Passage of Radiation through Matter

In particle physics, we describe the scattering of two particles in terms of the cross section. Consider a particle traveling parallel to a ‘target axis’ and offset by an impact parameter  $b$ , as in Figure 2.1:

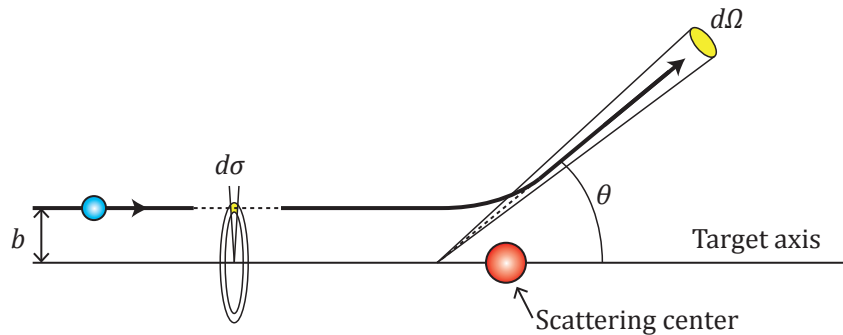


Figure 2.1: A particle incident in area  $d\sigma$  is scattered into solid angle  $d\Omega$ .

We see that a particle emanating from differential area  $d\sigma$  is scattered into solid angle  $d\Omega$  on interacting with the scattering center. Naturally,  $d\sigma$  and  $d\Omega$  are proportional to each other by some factor reflecting the strength of the interaction. This

proportionality factor is the differential cross section,  $D(\theta)$ :

$$D(\theta) = \frac{d\sigma}{d\Omega} . \quad (2.1)$$

We find the total cross section by integrating  $D(\theta)$  over all solid angles:

$$\sigma = \int d\sigma = \int D(\theta) d\Omega = \iint D(\theta) \sin \theta d\theta d\phi . \quad (2.2)$$

Of course,  $d\sigma$  and  $\sigma$  have units of area, hence the term ‘cross section’. However, the interpretation of  $d\sigma$  as a geometric cross-sectional area should not be confused with the real physical dimensions of the target. The scattering cross section is a hypothetical area that describes the likelihood of being scattered by the target.

In real materials, we have many scattering centers instead of a single target. To extend the example, consider a beam of particles with flux<sup>1</sup>  $F$  and cross-sectional area  $A$ , incident on a slab of material with a uniform number density of centers  $N$  and thickness  $\delta_x$ . Assuming  $\delta_x$  is small enough that the centers have a low chance to obscure each other, then the average number of particles scattered into solid angle  $d\Omega$  per unit time is

$$N_s(\Omega) = (F A)(N \delta_x) \frac{d\sigma}{d\Omega} , \quad (2.3)$$

and the total number of particles scattered into all angles per unit time is

$$N_{total} = \int N_s(\Omega) d\Omega = (F A)(N \delta_x) \sigma . \quad (2.4)$$

Dividing by  $(F A)$ , the total number of incident particles per unit time, then we have the probability of interaction for a single particle to be scattered in traversing a thickness  $\delta_x$ :

$$P_{int}(\delta_x) = (N \delta_x) \sigma . \quad (2.5)$$

## Mean Free Path

We want to consider the ‘survival probability’ for a particle to travel some thickness  $x$  without scattering:  $P_s(x)$ . If  $w dx$  is the probability of interacting over a distance  $dx$ , with  $w$  assumed constant, then the probability of *not* interacting over a length  $x + dx$  is

$$P_s(x + dx) = P_s(x) + \frac{dP_s}{dx} dx = P_s(x)(1 - w dx) , \quad (2.6)$$

---

<sup>1</sup>Incident particles per unit area, per time.

which yields

$$\frac{dP_s}{dx} = -wP_s(x) \quad \longrightarrow \quad P_s(x) = e^{-wx}, \quad (2.7)$$

and we see that the survival probability declines exponentially in distance. Likewise, we can express the probability of a particle scattering within the region  $x$  to  $x + dx$ , after traveling  $x$  without interacting, as

$$dP_{int}(x) = P_s(x)wdx = e^{-wx}wdx. \quad (2.8)$$

The mean free path,  $\lambda$ , is defined as the average distance traveled by a particle between successive scattering events; this is simply the expectation value of  $dP_{int}(x)$ ,

$$\lambda = \langle x \rangle \equiv \int_0^\infty x dP_{int} = \int_0^\infty w x e^{-wx} dx = \frac{1}{w}. \quad (2.9)$$

Thus, putting this result into (2.7), we find that

$$P_s(x) = e^{-x/\lambda}. \quad (2.10)$$

Intuitively,  $\lambda$  should be related to the number density of centers  $N$  and the total scattering cross-section of the medium,  $\sigma$ . In the limit of small  $\delta_x$ , we can use the Taylor series expansion of  $P_{int}(\delta_x) = 1 - P_s(\delta_x) = 1 - e^{-\delta_x/\lambda}$ :

$$\begin{aligned} P_{int}(\delta_x) &= 1 - \left(1 - \frac{\delta_x}{\lambda} + \mathcal{O}(\delta_x^2)\right) \\ &\simeq \frac{\delta_x}{\lambda}, \end{aligned} \quad (2.11)$$

which, when combined with (2.5), yields  $\lambda = 1/N\sigma$ .

### 2.1.1 The Bethe-Bloch Formula

The passage of charged particles through matter is generally characterized by energy loss and path deflection due to electromagnetic interactions with the nuclei and orbital electrons of the material. Specifically, inelastic collisions with atomic electrons may result in their excitation or ionization; this energy comes at the expense of the incident particle, causing it to slow down. In contrast, elastic collisions with atomic nuclei cause the incident particle to be deflected from its initial trajectory. Because the volume of an atom is primarily empty space, elastic scattering events from nuclei occur less frequently than inelastic collisions with atomic electrons.

We first treat energy loss due these inelastic collisions. Naturally, energy loss occurs not as a continuous process but in a discrete number of collisions. However, if a particle travels some path length  $l$  that is large compared to the mean free path  $\lambda$ , then we can account for the fluctuations in energy loss due to the statistical nature of collisions by working with the average energy loss per unit path length, or *stopping power*,  $dE/dx$ [9]:

$$-\frac{dE}{dx} = (2\pi N_a r_e^2 m_e c^2) \rho \frac{Z}{A} \frac{z^2}{\beta^2} \left[ \ln \left( \frac{2m_e \gamma^2 v^2 W_{max}}{I^2} \right) - 2\beta^2 - \delta - 2\frac{C}{Z} \right], \quad (2.12)$$

where the terms are

$N_a$	: Avogadro constant	$r_e$	: classical electron radius
$m_e$	: electron mass	$\rho$	: density of material
$Z$	: atomic number	$A$	: atomic weight
$\beta$	: $v/c$ of incident particle	$\gamma$	: $1/\sqrt{1 - \beta^2}$
$z$	: charge of incident particle in units of $e$	$C$	: shell correction
$I$	: mean excitation potential	$\delta$	: density correction
$W_{max}$	: maximum energy transfer in a single collision.		

Equation (2.12), commonly known as the *Bethe-Bloch* formula, is a quantum mechanical expression used for energy loss calculations. The mean excitation potential of the scattering material is the most critical Bethe-Bloch parameter; theoretically, it is the logarithmic average of the electron bound-state frequencies  $\nu$ , weighted by the oscillator strengths of the atomic levels. It is most often found semi-empirically[10].

For an incident particle with mass  $M$ , the maximum energy transfer in a single collision is[9]

$$W_{max} = \frac{2 m_e c^2 \eta^2}{1 + 2s\sqrt{1 + \eta^2} + s^2}, \quad (2.13)$$

where  $s = m_e/M$  and  $\eta = \beta\gamma$ . If  $M \gg m_e$ , then we then have

$$W_{max} \simeq 2m_e c^2 \eta^2. \quad (2.14)$$

The density correction and shell correction,  $\delta$  and  $C$ , become important at high and low velocities, respectively.

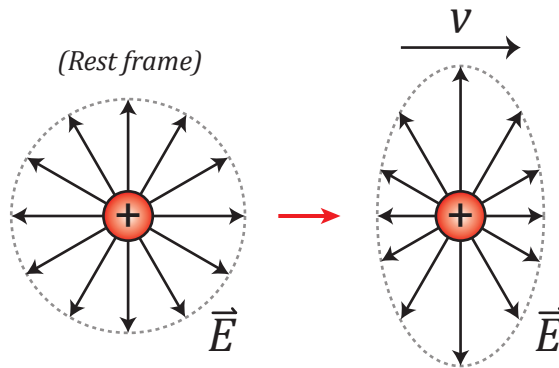


Figure 2.2: The electric field of a moving point charge is distorted by the Lorentz transformation.

## The Density Correction

The electric field of a charged particle moving with relativistic speed becomes flattened and extended in the plane perpendicular to its direction of travel due to the Lorentz transformation, as shown in Figure 2.2. In a sense, the warping of the electric field increases stopping power by contributing distant-collision terms, transverse to the particle's motion, which otherwise would have had a lesser effect. However, the electric field of the particle also tends to polarize atoms along its path, and so electrons far from the incident particle will be shielded from the full field intensity. This damping of the anticipated rise in stopping power for relativistic particles is so-named the *density effect* because it depends on the density of the material.

The values of  $\delta$  are usually computed using Sternheimer's parametrization[11]:

$$\delta = \begin{cases} 0 & X < X_0 \\ 4.6052X + C_0 + a(X_1 - X)^m & X_0 < X < X_1 \\ 4.6052X + C_0 & X > X_1 \end{cases}, \quad (2.15)$$

where  $X = \log_{10}(\beta\gamma)$  and  $C_0$  is defined as

$$C_0 = -\left(2 \ln \frac{I}{h\nu_p} + 1\right), \quad (2.16)$$

and where  $h\nu_p$  is the plasma frequency of the material with electron density  $N_e$ ,

$$\nu_p = \sqrt{\frac{N_e e^2}{\pi m_e}}. \quad (2.17)$$

The remaining parameters are found by fitting (2.15) to experimental data.

## The Shell Correction

When the velocity of the particle is slowed to be comparable to the orbital velocity of bound electrons, the electrons can no longer be assumed stationary with respect to the particle, an explicit assumption of the Bethe-Bloch formula. An empirical correction is used in this regime[12], valid for  $\eta \geq 0.1$ :

$$C(I, \eta) = (0.422377\eta^{-2} + 0.0304043\eta^{-4} - 0.00038106\eta^{-6}) \times 10^{-6} I^2 + (3.850190\eta^{-2} - 0.1667989\eta^{-4} + 0.00157955\eta^{-6}) \times 10^{-9} I^3, \quad (2.18)$$

recalling that  $\eta = \beta\gamma$  and  $I$  is the mean excitation potential, in eV.

### 2.1.2 Energy Loss of Electrons and Positrons

Like other charged particles, electrons and positrons suffer collisional energy losses when passing through matter. However, due to their small mass, they can lose significant energy due to the emission of electromagnetic radiation as they are decelerated by the electric field of a nucleus. This braking radiation or *bremsstrahlung* quickly dominates energy losses at energies above a few 10's of MeV[9]. The total stopping power is then composed of radiative and collisional losses,

$$\left( \frac{dE}{dx} \right)_{total} = \left( \frac{dE}{dx} \right)_{rad} + \left( \frac{dE}{dx} \right)_{coll}, \quad (2.19)$$

and the material-specific critical energy  $E_c$  is defined as the energy at which radiative and collisional losses are equal to each other.

The collisional term, based on the Bethe-Bloch formula, must be modified to account for the fact that electrons are indistinguishable particles. In particular, the maximum energy transfer due to a head-on collision is now  $W_{max} = T_e/2$ , where  $T_e$  is the kinetic energy of the incident electron[10]. Positrons, which are not subject to this limitation, have  $W_{max} = T_p$  with incident kinetic energy  $T_p$ . The modified

Bethe-Bloch formula for collisional losses is then

$$-\left(\frac{dE}{dx}\right)_{\text{coll}} = (2\pi N_a r_e^2 m_e c^2) \rho \frac{Z}{A} \frac{1}{\beta^2} \left[ \ln \left( \frac{\tau^2(\tau+2)(m_e c^2)^2}{2I^2} \right) - F^\pm(\tau) - \delta - 2 \frac{C}{Z} \right], \quad (2.20)$$

where  $\tau$  is the kinetic energy of the particle in units of  $m_e c^2$ , and  $F(\tau)$  is given by

$$\begin{aligned} F^-(\tau) &= 1 - \beta^2 + \frac{\frac{\tau^2}{8} - (2\tau + 1)\ln 2}{(\tau + 1)^2}, \\ F^+(\tau) &= 2\ln 2 - \frac{\beta^2}{12} \left( 23 + \frac{14}{\tau + 2} + \frac{10}{(\tau + 2)^2} + \frac{4}{(\tau + 2)^3} \right), \end{aligned} \quad (2.21)$$

for electrons and positrons, respectively[9].

## Radiative Losses

Because radiative losses depend on the electric field felt by the electron, the screening of the nucleus' electric field by atomic electrons plays an important role. As such, the bremsstrahlung cross-section is dependent on the electron's energy, its impact parameter, and the atomic number of the material,  $Z$ . Screening is parametrized by the quantity

$$\xi = \frac{100 m_e c^2 h\nu}{E_0 E Z^{1/3}}, \quad (2.22)$$

where  $E_0$  is the particle's total initial energy and  $E$  is its final total energy, and  $h\nu$  is the energy of the emitted photon. For complete screening,  $\xi \simeq 0$ , and for no screening,  $\xi \gg 1$ . The bremsstrahlung cross-section is given by the formula[9]

$$\begin{aligned} d\sigma = 4Z^2 r_e^2 \alpha \frac{d\nu}{\nu} \left\{ (1 + \epsilon)^2 \left[ \frac{\phi_1(\xi)}{4} - \frac{1}{3} \ln Z - f(Z) \right] \right. \\ \left. - \frac{2}{3} \epsilon \left[ \frac{\phi_2(\xi)}{4} - \frac{1}{3} \ln Z - f(Z) \right] \right\}, \end{aligned} \quad (2.23)$$

where  $\epsilon = E/E_0$ ,  $\alpha = 1/137$ ,  $f(Z)$  is a small correction accounting for the Coulomb interaction of the emitting electron in the electric field of the nucleus, and  $\phi_1$ ,  $\phi_2$  are screening functions depending on  $\xi$ :

$$\begin{aligned}\phi_1(\xi) &= 20.863 - 2 \ln[1 + (0.55846\xi)^2] - 4[1 - 0.6e^{-0.9\xi} - 0.4e^{-1.5\xi}] , \\ \phi_2(\xi) &= \phi_1(\xi) - \frac{2}{3}(1 + 6.5\xi + 6\xi^2)^{-1} ,\end{aligned}\quad (2.24)$$

and where

$$f(Z) \simeq a^2 [(1 + a^2)^{-1} + 0.20206 - 0.0369a^2 + 0.0083a^4 - 0.002a^6] \quad (2.25)$$

for  $a = Z\alpha$ .

The energy loss due to radiation is then calculated by integrating the cross section  $d\sigma/d\nu$  times the photon energy  $h\nu$  over the allowed frequency range,

$$-\left(\frac{dE}{dx}\right)_{rad} = N \int_0^{\nu_0} h\nu \frac{d\sigma}{d\nu} d\nu \quad (2.26)$$

where  $N$  is the number of atoms per cubic centimeter, and  $\nu_0 = E_0/h$ .

### 2.1.3 NIST EStar Database

The National Institute of Standards and Technology (NIST) has available three computer-readable databases for calculating stopping power-related data. These are EStar, PStar, and AStar, for electrons, protons, and helium ions, respectively. The EStar program calculates collisional and radiative losses, density corrections, and the total stopping power for electrons (or positrons) traveling through any one material from a list of hundreds of common compounds.

The method of EStar's calculation follows the Bethe-Bloch formula (2.20) with the material-specific density correction (2.15) and mean excitation potential  $I$ . EStar does not include a shell correction, meaning that collisional loss uncertainties increase from between 1% and 2% above 100 keV, to between 5% and 10% from 100 keV to 10 keV. This is not a concern because the energy range below 100 keV is only .2% of the range we are interested in (up to 52.5 MeV). Radiative losses are calculated through a combination of bremsstrahlung cross sections[13], numerical results in the sub-2 MeV range[14], analytical formulas above 50 MeV, and interpolation in the intermediate 2-50 MeV range.

In Figure 2.3, we see that the radiative losses increase for higher-energy electrons, but that collisional losses still dominate in the range of interest below 52.5 MeV;

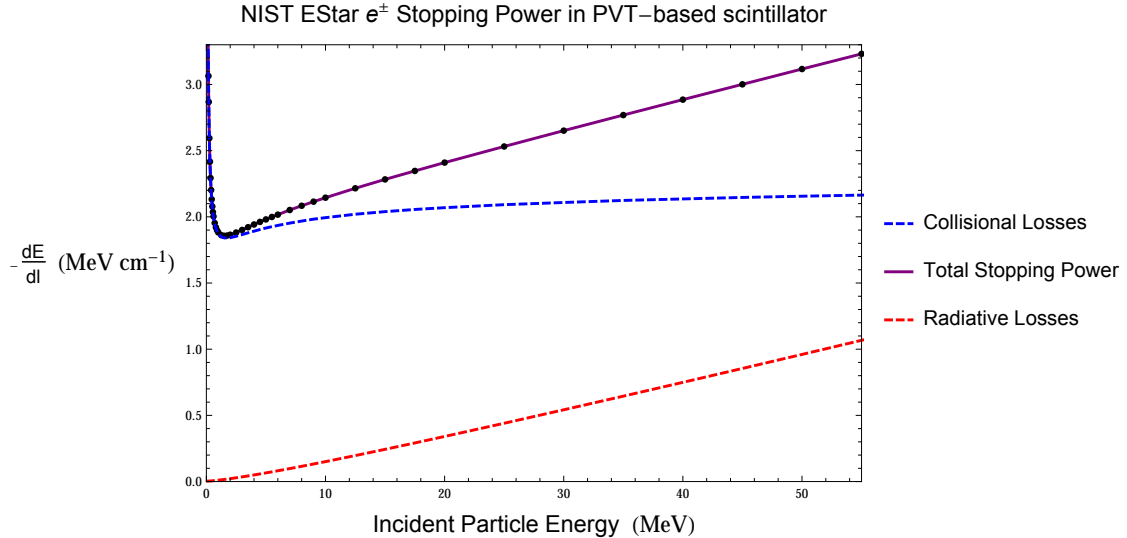


Figure 2.3: The collisional, radiative, and total stopping power of electrons and positrons in polyvinyltoluene-based scintillator, calculated from the NIST EStar database.

evidently, we are below the critical energy  $E_c$ . If we assume that the rate of energy loss at every point along the path of a charged particle is equal to the total stopping power, then we can estimate the range of a particle by integrating the reciprocal stopping power over energy as

$$\Delta x = \int_0^{E_0} \left( -\frac{dl}{dE} \right) dE . \quad (2.27)$$

This value, called the continuous-slowing-down approximation range (CSDA range), is a very close estimate to the average path length that a particle of energy  $E_0$  travels as it slows down to rest. The validity of the CSDA approximation is of course limited to ranges for which  $\Delta x \gg \lambda$ , such that the fluctuations in energy loss average out as presupposed in the Bethe-Bloch formula.

#### 2.1.4 The Landau-Vavilov Distribution

The stopping power represented by the Bethe formula describes the mean rate of energy loss as weighted over all types of collisions. For any given particle, however, the deposited energy will not be equal to the integrated stopping power over its trajectory, due to statistical fluctuations in the number of collisions suffered and the energy transferred in each case. We parameterize energy loss fluctuations with

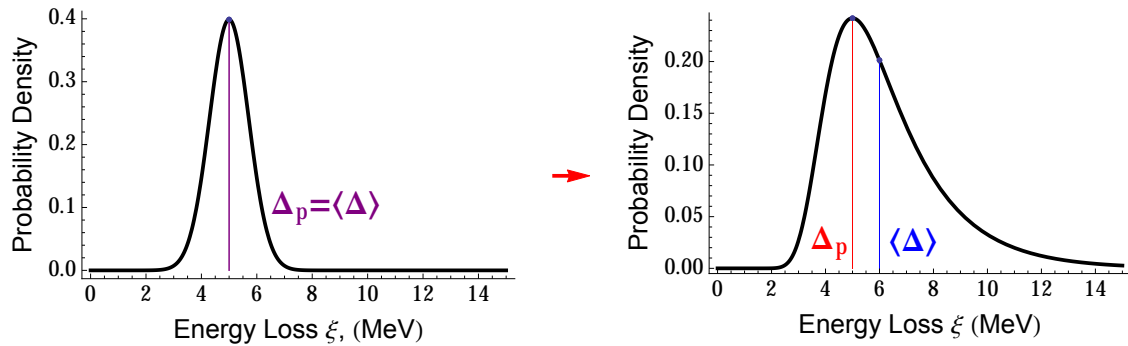


Figure 2.4: Probability density functions modeling energy loss fluctuations in thick (left) and thin (right) absorbers. On the left, the number of large-energy-transfer collisions is small compared to the total number of collisions; the *pdf* is approximately Gaussian. On the right, large-energy-transfer collisions skew the *pdf* such that the mean and most probable energy loss no longer coincide:  $\Delta_p \neq \langle \Delta \rangle$ .

Landau's parameter

$$\kappa = \frac{\bar{\Delta}}{W_{max}}, \quad (2.28)$$

where  $\bar{\Delta}$  is the mean energy loss, and  $W_{max}$  is the maximum allowed energy transfer in a single collision.  $\kappa$  describes the contribution of high-energy-transfer collisions close to  $W_{max}$ .

A large value of  $\kappa$  implies that the total energy loss is composed of a large number of small-energy-transfer collisions. By the Central Limit Theorem<sup>2</sup>, energy loss fluctuations are described by a symmetric Gaussian probability density function (*pdf*). The Gaussian *pdf* is valid for nonrelativistic particles or large thicknesses, often given by  $\kappa > 10$ ; the Bethe formula is valid by symmetry of the *pdf*[15].

For materials of moderate thickness ( $\kappa < 10$ ), energy loss fluctuations are instead described according to Landau's theory[16] by a skewed-asymmetric Gaussian with a long, high-energy tail, due to the possibility of single collisions with large-energy-transfer. This effect is especially significant for electrons, which can lose up to half their kinetic energy in a single collision. In the right side of Figure 2.4, we see that the mean and most probable energy losses no longer coincide, as they would in a thick absorber with large  $\kappa$ .

<sup>2</sup>The arithmetic mean of a large number of iterates of independent variables will be normally distributed, regardless of the underlying distribution.

## 2.2 Scintillation

Scintillators are materials that respond to the energy loss of particles by reemitting the deposited energy as light. This prompt emission of light in response to excitation is called *fluorescence*; it is a property shared by all scintillators, and is the reason for their widespread use as particle detectors.

The six primary types of scintillators in use today are: organic crystals, organic liquids, plastics, inorganic crystals, gaseous scintillators, and glasses. Even within each type, there are many different choices of compounds available, depending on the intended use of the scintillator. Plastics are the general ‘workhorse’ scintillator in nuclear and particle physics, due to their extremely fast signals, relatively cheap cost, and the ease with which they are molded and machined into different shapes. As the detector in this experiment uses plastic scintillator, we limit discussion to this class of material.

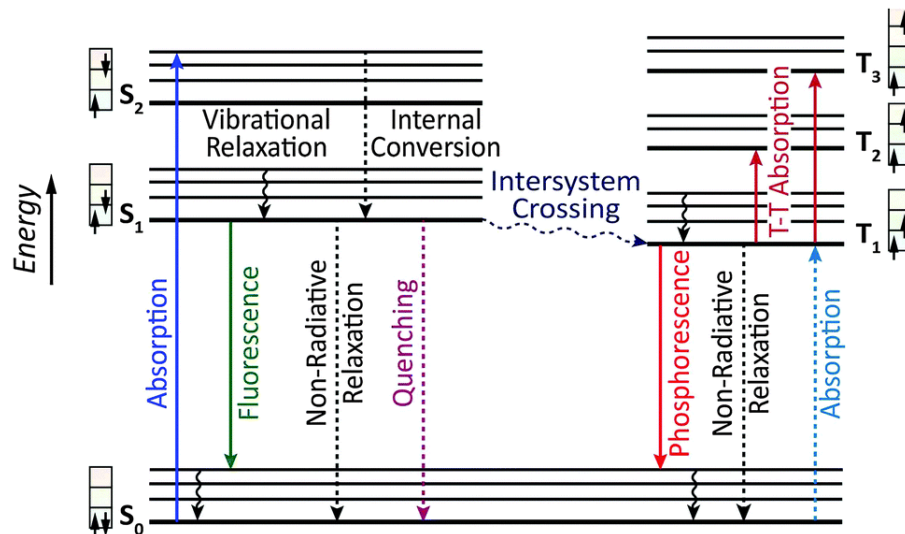


Figure 2.5: Energy level diagram of excitation and luminescence processes in an organic molecule with  $\pi$ -electronic structure. (From H. Xu, R. Chen, Q. Sun, W. Lai, Q. Su, W. Huang, and X. Liu, *Recent progress in metal-organic complexes for optoelectronic applications*, Chem. Soc. Rev. 2014, 43, 3259-3302. Published online 2/17/2014, Creative Commons License.)

In organic scintillators, the fluorescence mechanism is based on transitions in the energy level of a single molecule, and is independent of the phase of the material or its lattice structure. Many organic scintillators are based on molecules with  $\pi$ -electron structure. In Figure 2.5, we see that a molecule with such structure has a series of singlet states  $S_0, S_1, S_2, \dots$ , and a similar set of triplet states  $T_1, T_2, \dots$ , both of which are subdivided into further levels corresponding to the vibrational modes of the

molecule. Because the spacing between vibrational states (on the order of 0.15 eV) is large compared to average thermal energies (0.025 eV), nearly all such molecules are in the ground state  $S_{0,0}$  at room temperature[17].

When a charged particle passes nearby, the scintillating molecule can absorb some of its kinetic energy and be excited into a higher electronic state. The higher-energy singlet states rapidly de-excite to the  $S_1$  state by radiationless internal conversion, and any excess vibrational energy is quickly lost to thermal equilibrium[17]. As such, the effect of a charged particle passing through a scintillator is to rapidly produce populations of excited molecules in the  $S_{1,0}$  state.

Fluorescence occurs when the molecule transitions from the  $S_{1,0}$  state to one of the vibrational states of  $S_0$ , emitting a photon. This principal mode of scintillation is called the *prompt* component, as it is the fastest mode of reemission, occurring within  $10^{-8}$  s after absorption[9]. However, some of the  $S_{1,0}$  excited states can transition<sup>3</sup> to the first triplet state  $T_1$ , which has a characteristically longer lifetime (as long as  $10^{-3}$  s) than the  $S_1$  state.<sup>4</sup> The de-excitation of the molecule from  $T_1$  to  $S_{0,n}$  then results in a *delayed* component, commonly referred to as phosphorescence. Importantly, the energy of fluorescence and phosphorescence emissions are lower (their arrows in Figure 2.5 are shorter) than the minimum energy required for excitation; there is then little overlap between the absorption and emission spectra for scintillating molecules, allowing them to be partially transparent to their own emission.

Plastic scintillators consist of a ‘base’ structural plastic with additive fluorescent emitters or ‘fluors’ suspended throughout the base. Ionization in the base plastic produces UV photons with an attenuation length of several millimeters.<sup>5</sup> The fluors are added in a concentration (typically 1% by weight) such that the average distance between a fluor and base molecule is  $\sim 100$  Å, much less than a wavelength of light. At this distance, the energy transfer from excited base to fluor occurs by the Forster resonance energy transfer, a dipole-dipole interaction with strong coupling that is much faster and more efficient than energy transfer by radiation of a photon[10]. The additive fluors function as “wavelength shifters,” re-emitting energy in the visible spectrum to which the base plastic is more transparent.<sup>6</sup> This method results in a scintillator

---

<sup>3</sup>Via *intersystem crossing*, a radiationless process between electronic states with different spin multiplicity.

<sup>4</sup>It is also possible for molecules in the  $T_1$  state to be excited back to the  $S_1$  state and subsequently de-excite via prompt fluorescence.

<sup>5</sup>The attenuation of photons in the base is due to the small but nonzero overlap between absorption and emission spectra as previously described.

<sup>6</sup>Secondary fluors are sometimes introduced at fractional percent levels to further shift the emission wavelength from that of the primary fluor, which may function well in its coupling to the base

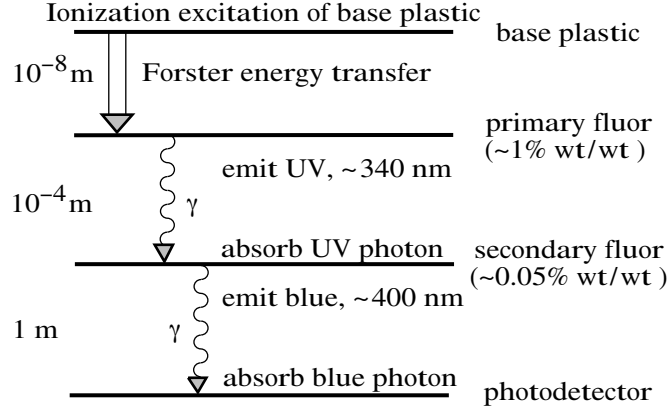


Figure 2.6: The working mechanism of a ternary-solution plastic scintillator, with approximate fluor concentrations (in weight percentage) and energy transfer distances of the sub-processes. (From K.A. Olive *et al.* (Particle Data Group), Chin. Phys. C, **38**, 010009 2014)

with little self-absorption, high light-yield, and very fast decay times.

Assuming that the excited molecules rapidly settle into  $S_{1,0}$ , then the fluorescence process is approximated by the exponential decay

$$R(t) = \frac{N_0}{\tau_p} e^{-t/\tau_p}, \quad (2.29)$$

where  $R(t)$  is the rate of photons emitted at time  $t$ ,  $N_0$  is the total number of photons emitted, and  $\tau_p$  is the ‘prompt’ decay constant of the  $S_{1,0}$  state. Knowing that the  $T_1$  state has a longer lifetime than the  $S_{1,0}$  state, it is clear that the total light decay curve should be the sum of the prompt and delayed components due to fluorescence and phosphorescence, respectively:

$$R(t) = Ae^{-t/\tau_p} + Be^{-t/\tau_d}, \quad (2.30)$$

where  $\tau_d$  is the delayed decay constant of the  $T_1$  state. Such a curve is represented in Figure 2.7; the relative magnitudes  $A$  and  $B$  vary by material and by the type of incident particle[9].

## Linearity and Efficiency

In reality, only a small fraction of a particle’s kinetic energy is converted to light by the scintillation mechanism; the remainder is lost primarily to lattice vibrations

---

molecules but re-emits at an inconvenient wavelength.

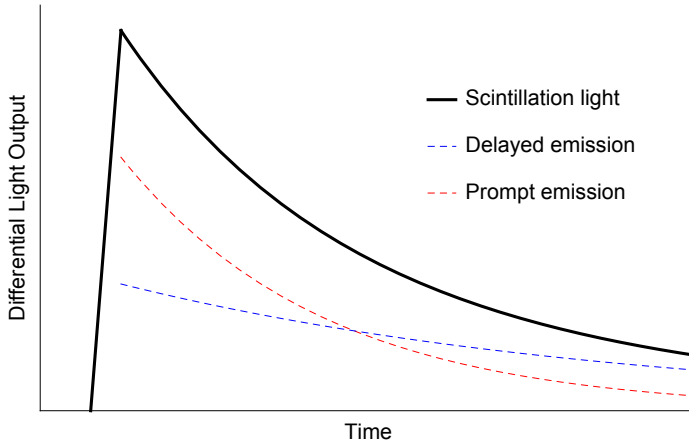


Figure 2.7: The composite light yield of a scintillator, represented by the sum of two exponential decays— the prompt and delayed components.

or heat. We name this fraction the scintillation efficiency,  $S$ . The light response of organic scintillators to charged particles is a complex process and depends on both the particle type and its energy. However, for electrons with energies above  $\sim 125$  keV the response is approximately linear[17]:

$$\frac{dL}{dx} = S \frac{dE}{dx}, \quad (2.31)$$

where  $dL/dx$  is the fluorescent energy emitted per unit path length, and  $dE/dx$  is the electron's specific energy loss. For heavier and more energetic particles, the relation between light emitted and energy lost becomes more complicated.

## 2.3 Photomultiplier Tubes

Photomultiplier tubes (or PMTs, for short) convert the light pulse of a scintillator into a readable electronic signal for analysis. Importantly, PMTs are sensitive enough to detect weak light pulses,<sup>7</sup> and sometimes single photons, with very little noise amplification. They accomplish this by first converting photons into photoelectrons at the *photocathode*. These ‘primary electrons’ then pass through the *electron multiplier* structure, where they are greatly amplified in number and collected at the anode, causing a pulse in current. In general, this amplification is linear, meaning that the strength of the PMT’s output signal is proportional to the number of incident photons.

<sup>7</sup>which can consist of no more than a few hundred photons

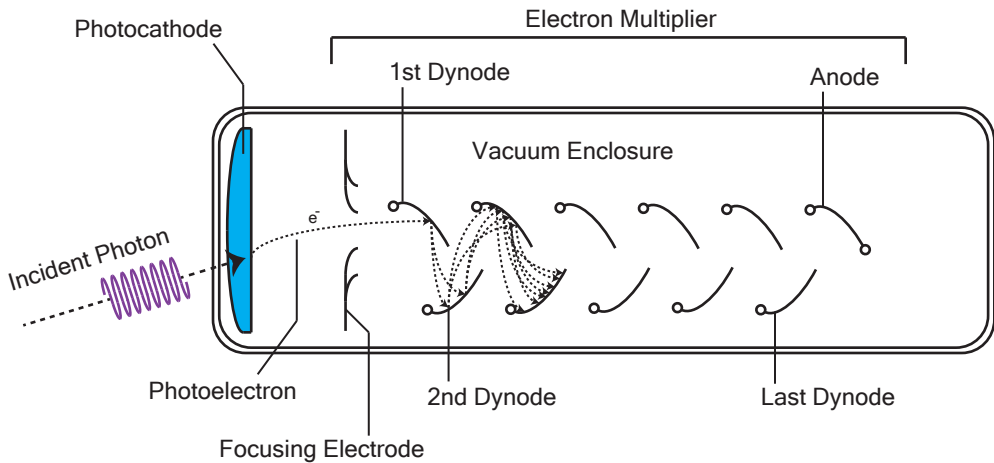


Figure 2.8: Basic elements of a photomultiplier tube.

### 2.3.1 The Photocathode

At the photocathode, photons are converted to electrons via the photoelectric effect. This process occurs when an incident photon is absorbed, and its energy  $E = h\nu$  is transferred to an electron in the photocathode. The electron then migrates to the surface of the photocathode, losing some of its energy to electron-electron collisions. If the electron has sufficient energy left to overcome the material's work function  $\phi$ , then it is emitted with kinetic energy

$$E < h\nu - \phi . \quad (2.32)$$

The work function  $\phi$  represents the inherent potential barrier that exists at any material-vacuum interface. It is clear that  $\phi$  imposes a minimum frequency on  $\nu$ , below which the photoelectric effect cannot occur. Even above this threshold, however, the photocathode is an imperfect emitter; depending on the path the electrons take, some may lose enough energy to be unable to escape. As such, photocathodes are delicately optimized to have a high escape depth<sup>8</sup> while remaining (mostly) opaque to photons; if the photocathode is too thin, it may be too transparent to photons, despite having a relatively high efficiency for emitting photoelectrons. Evidently,

---

<sup>8</sup>The depth in the material at which electrons may originate and still reach the surface with sufficient energy to escape

photocathodes have an intrinsic quantum efficiency

$$\eta(\lambda) = \frac{\# \text{ of photoelectrons emitted}}{\# \text{ of incident photons of wavelength } \lambda}, \quad (2.33)$$

which for most applications reaches its maximum at about 20-30%.

An important consequence of the photocathode's high sensitivity (low- $\phi$ ) is the phenomenon of spontaneous electron emission. Electrons in the conduction band of the photocathode carry some thermal kinetic energy, and, on average, this energy is lower than  $\phi$ . However, the spread of their distribution may be large enough that electrons at the extreme high-end will have thermal kinetic energy greater than  $\phi$ . If these electrons are also near the photocathode surface, they can spontaneously escape, propagate through the electron multiplier, and be read as a weak output signal. The presence of these spontaneous, thermally-induced signals is called *thermionic noise* or *dark count*. Importantly, these are ‘single-electron events’; they are the weakest possible signals to be detected by the PMT. We will see that single-electron events have a characteristic pulse height spectrum, due to the statistical nature of electron multiplication and the properties of the PMT itself.

### 2.3.2 Electron Multiplier

The electron multiplier structure consists of a chain of electrodes called *dynodes*. At each dynode, a single high-energy electron is able to liberate several low-energy electrons via secondary electron emission. In this process, electrons in the dynode material are excited into the conduction band by the passage of an incident energetic electron. Similar to the photoelectric effect in the photocathode, these excited electrons then migrate to the surface and, if they have sufficient energy, are able to escape the dynode.

The multiplication factor for a single dynode is defined as

$$\delta = \frac{\# \text{ of secondary electrons emitted}}{\text{incident electron}}, \quad (2.34)$$

and is generally a sensitive function of the incident electron’s energy[17]. This is because, for incident low-energy electrons, relatively fewer material electrons will be excited to the conduction band. Nevertheless, these excited electrons will also be formed closer to the dynode surface, due to the low penetrative power of the primary electron. On the other hand, incident high-energy electrons can excite more material electrons, but at greater average depth, and thus having lower probability of escape.

By holding each dynode at a higher potential than the preceding one, low-energy electrons escaping one dynode are guided and accelerated by the electrostatic field to hit the following one. With an inter-dynode potential difference of  $\sim 100$  V, the electrons are accelerated to high enough energy such that, on striking the next dynode, they again free multiple low-energy electrons via secondary emission. This process is repeated many times in order to achieve gains on the order of  $10^6$  -  $10^7$ ; with the dynodes arranged into  $N$  stages, the overall gain of the PMT is approximately

$$g = \alpha \delta^N , \quad (2.35)$$

where  $\alpha$  is the fraction of all photoelectrons captured at the first dynode. The first three stages of electron multiplication are depicted in Figure 2.8 (in this case,  $\delta = 2$ ).

The inter-dynode voltages differences are typically maintained by a high-voltage source applied across a resistive voltage divider circuit. Because  $\delta$  is function of the incident electron's energy, it is also implicitly a function of the inter-dynode voltage difference  $V$ . Therefore, the overall gain  $g$  is a highly sensitive function of  $V$ .<sup>9</sup>

### 2.3.3 Single-Photoelectron Statistics

From the statistical nature of secondary electron emission, we know that the multiplication factor  $\delta$  is not strictly constant for any particular dynode. If  $\delta$  were constant, then every photoelectron would be subject to the exact same multiplication, and there would be a one-to-one correspondence between the output pulse height and the original number of photoelectrons. In reality, when a PMT measures light pulses from a source of constant intensity, there is some variation in the output pulse height, symmetric about a central peak. This distribution in pulse heights is due to fluctuations in  $\delta$ .

The pulse height spectrum for single-photoelectron events characterizes the degree of fluctuations in  $\delta$  and the collective statistics of the electron multiplier. It also helps us understand certain artifacts in the low-end of the energy spectrum. In the simplest model, we assume that the production of secondary electrons at a given dynode is Poisson-distributed about the average yield,  $\delta$ . The variance of a Poisson distribution is equal to its expected value,  $\delta$ , and so the standard deviation is  $\sigma = \delta^{1/2}$ . The relative variance, defined as  $(\sigma/\delta)^2$ , is then equal to  $1/\delta$ . When the process is compounded over  $N$  dynode stages, it can be demonstrated[17] that the relative variance in the

---

<sup>9</sup>For example, if  $\delta$  were a linear function of  $V$  in a 10-stage PMT, then the overall gain  $g$  would vary as  $V^{10}$ .

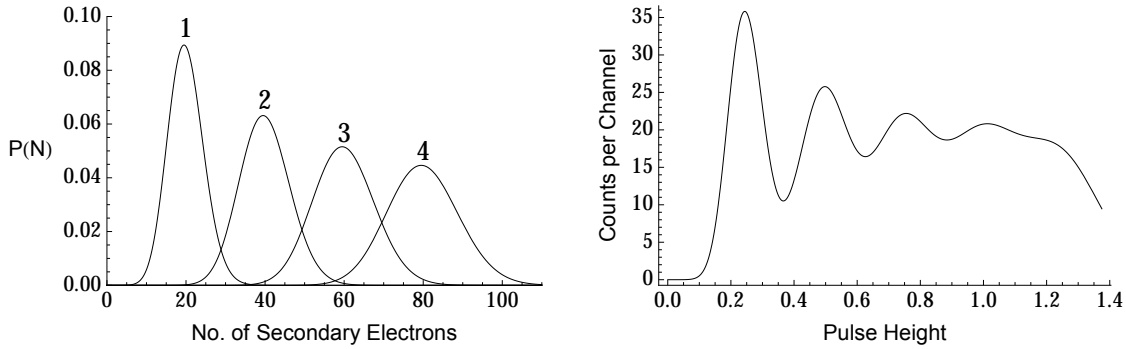


Figure 2.9: Left: Probability distributions of secondary electron emission at the first dynode of a PMT, due to 1,2,3, and 4 incident photoelectrons. Statistical broadening of  $P(N)$  increases as the number of photoelectrons increases. Right: Low-end of a simulated pulse height spectrum of a PMT. At low pulse heights, the dependence on the first dynode's  $\delta$  results in distinguishable peaks corresponding to 1, 2, and 3 photoelectron events.

number of secondaries produced is

$$\frac{1}{\delta} + \frac{1}{\delta^2} + \frac{1}{\delta^3} + \dots + \frac{1}{\delta^N} \simeq \frac{1}{\delta - 1}. \quad (2.36)$$

Thus, when  $\delta \gg 1$ , we see that the relative variance in the output pulse height is dominated by the fluctuations in  $\delta$  at the first dynode. This is perfectly intuitive; the number of electrons emitted at the first dynode should have the greatest ‘impact’ on the ability of the following  $N - 1$  dynodes to produce electrons.

As a consequence of the pulse height’s dependence on  $\delta$ , it is sometimes possible to resolve distinct peaks corresponding to low-photoelectron events at the first dynode. On the left side of Figure 2.9, we see the statistical broadening of  $\delta$  is smallest for single-photoelectron events, and increases as we go up to 2, 3, 4, ... photoelectrons. If  $\delta$  is sufficiently large, then the broadening by variance  $1/\delta$  may be small enough to distinguish peaks in the distribution corresponding to discrete numbers of photoelectrons, as shown on the right side of Figure 2.9. This artifact is an important consideration for weak scintillation events, where the low-photon signals may be confounded with thermionic emissions.

# Chapter 3

## Detector Design and Experimental Procedure

### 3.1 Apparatus

The scintillation detector used for this experiment was designed by Eljen Technology in Sweetwater, Texas. It consists of a cylindrical (40 cm tall, 10 cm in radius) EJ-200 plastic scintillator coupled to an ETEL 9390KB photomultiplier tube via a 4-inch thick PMMA light guide. The scintillator and light guide are both wrapped in a light-tight black vinyl cover with an internal reflective layer for collection efficiency.

EJ-200 is a Polyvinyl-Toluene (PVT) based scintillator that is doped with Anthracene as a primary fluor. Like most plastics, EJ-200 has very fast timing, with a decay time of 2.1 ns. Its emission spectrum is well-matched to the 9390B's quantum efficiency profile. The 9390B has 10 dynodes, providing a gain of  $g = 7 \times 10^5$  when powered at 1000V. It has two signal outputs available: the anode, and the last dynode. We use the signal from the last dynode, which is better for energy information.

For the purposes of the experiment, it is important that the PMT produce consistently sized pulses when detecting electrons of the same energy, regardless of their location in the scintillator. This is a challenge because, as the scintillation light is emitted in all directions, only a fraction will travel directly to the PMT window; the remainder is reflected internally at one or more surfaces of the scintillator before it is collected. At each reflection, there is a chance for photons to escape, and optical attenuation becomes more likely the further the photons are made to travel. As such, for decays occurring near the PMT, a greater fraction of the light is absorbed directly than for decays of equal energy that occur far from the PMT. Therefore, if

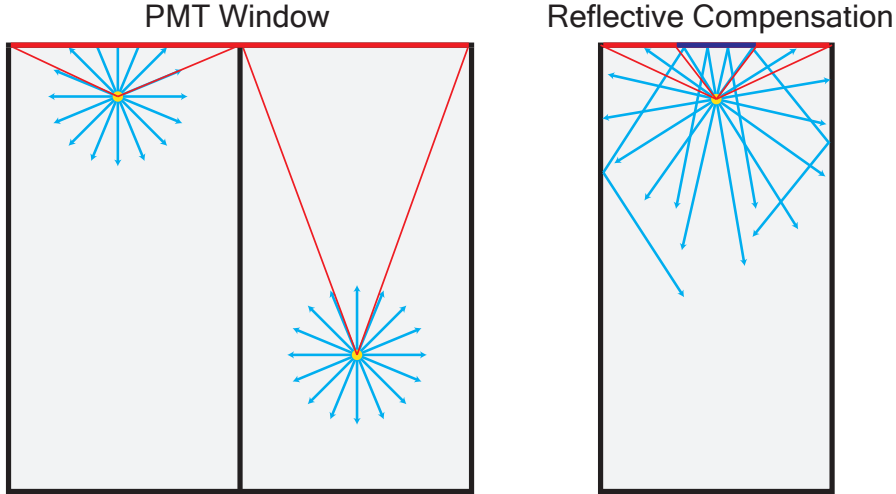


Figure 3.1: Compensating the light collection for near-PMT events by a reflective shield.

not compensated for in the detector's design, these near-PMT events will appear to be higher energy than far-PMT events.

Compensation for this effect is done by adding a reflective circle at the window of the PMT, which forces the direct photons to take a longer path before being collected. Figure 3.1 illustrates the greater fraction of light collected by near-PMT decays, and the principle of reflective compensation.

The last piece of equipment is the Tektronix TDS 744A digitizing oscilloscope, which we use for data acquisition. The oscilloscope monitors the dynode output signal of the PMT, sampling at a rate of 2 GS/s or .5 ns per sample. This allows us to resolve the very fast PMT pulses, with FWHM of  $\sim 25$  ns, into enough data points for later analysis. An NI LabVIEW program was developed to communicate with the oscilloscope and search for decay events in the PMT signal.

## The Experiment

The principle of the experiment is as follows: A muon created in the upper atmosphere travels to sea level due to the effect of time dilation, where it is incident on our detector. In most cases, the muon is so energetic that it passes straight through the scintillator volume, depositing some energy and producing one pulse as in Figure 3.2a.

If the muon has sufficiently low energy, it may be stopped in the detector. The stopped  $\mu^\pm$  decays an average  $2.2 \mu\text{s}$  later to produce an  $e^\pm$  and two neutrinos. The neutrinos escape undetected, but the  $e^\pm$  deposits more energy in the scintillator as

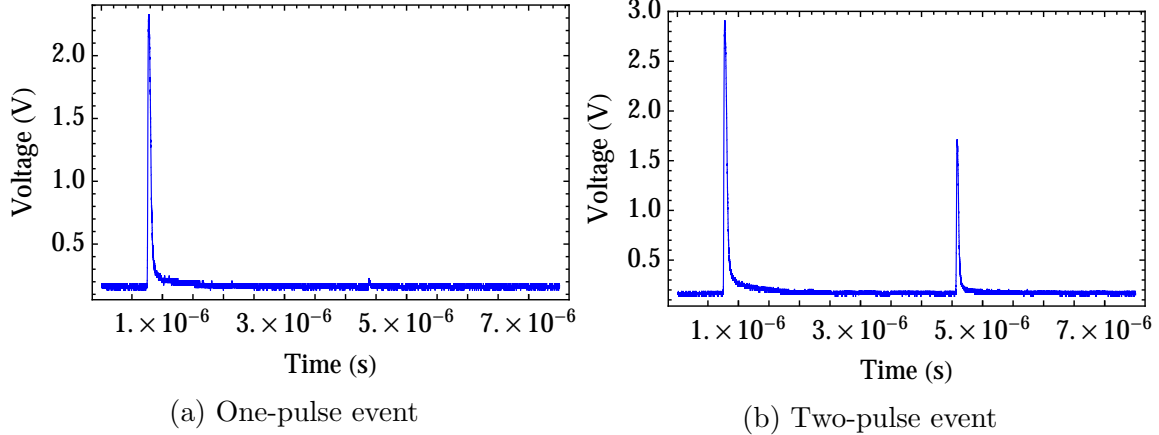


Figure 3.2: The PMT’s dynode output signal for two events: (a) A muon passing straight through the detector, and (b) A muon enters with low energy, is brought to rest, and decays to produce an electron, which generates a second pulse.

it, too, is slowed by matter. A decay event then registers as two pulses in the PMT signal, as in Figure 3.2b.

The energy of the decay product  $e^\pm$  is determined probabilistically by the approximate Fermi distribution from Chapter 1,

$$P(E_e) = C(m_\mu c^2 E_e)^2 \left( 3 - 4 \frac{E_e}{m_\mu c^2} \right). \quad (3.1)$$

Assuming that the scintillator’s light output response is linearly related to the deposited energy, and that the PMT amplifies pulses in a linear manner, we then ‘measure’  $E_e$  by associating it with the integrated area under its pulse.

If we could observe a large number of these decays, we might compare the data to (3.1) and extract  $m_\mu$  as a fit parameter. The primary difficulty is that, depending on where the decay occurs and in which direction the  $e^\pm$  travels, it may escape the scintillator volume and deposit only a fraction of its energy, therefore appearing to have lower energy than its ‘true’ value. This ‘electron-escape’ effect distorts the observed energy spectrum from the ideal distribution of (3.1) to that shown on the right in Figure 3.3. Because higher-energy  $e^\pm$  are more likely to be produced, and, with their longer range, are also more likely to escape, this effect disproportionately shifts higher-energy events to the low-energy end of the spectrum.

Electron-escape is a geometric effect that is manifested statistically over a large number of events; there is no analytic way to extract  $m_\mu$  from the shifted distribution in Figure 3.3, which is the distribution we observe experimentally. To account for electron-escape, we use a Monte Carlo method to produce a large number of random

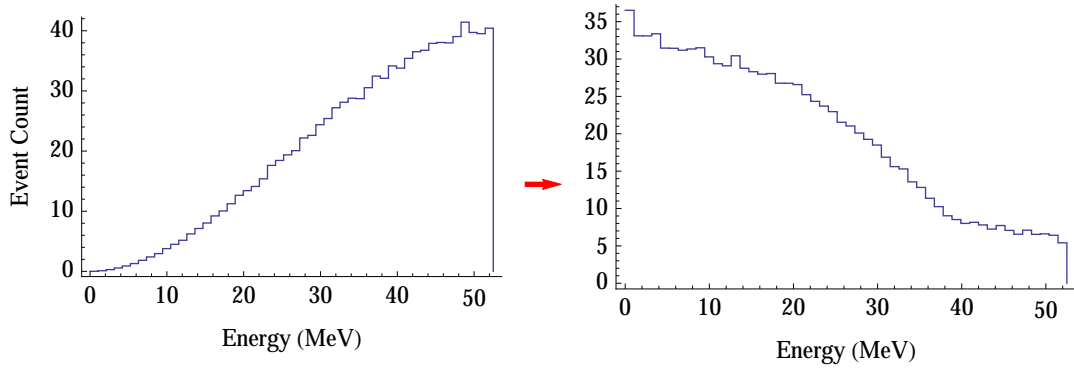


Figure 3.3: The energy spectra of  $e^\pm$  emitted in muon decay, in an ‘ideal’ scintillator with infinite volume (left) and the ‘real’ scintillator with finite volume (right). The effect of electron-escape obscures the underlying distribution of energy,  $P(e^\pm)$ .

events and simulate their energy deposition in the detector, giving us a simulated distribution of  $e^\pm$  energy. Of course, each simulated distribution assumes some value for  $m_\mu$ , from which the initial energies of the  $e^\pm$  are sampled. If the detector simulation accurately describes the physics of  $e^\pm$  energy loss, and if the choice of  $m_\mu$  appreciably changes the qualitative shape of the energy distribution (as we might expect), then we can measure  $m_\mu$  by comparing the observed distribution to those simulated at different values of  $m_\mu$ . Whichever  $m_\mu$ -simulated distribution to most closely match the observed data is then the true value of  $m_\mu$ .

## 3.2 Data Acquisition in NI LabVIEW

NI LabVIEW communicates directly with the TDS 744A oscilloscope via a GPIB port. To get the most information from the decay signals, we sample at the maximum rate of 2 GS/s. While the oscilloscope is technically capable of sampling at higher rates, it requires multiple sampling of a periodic signal to do so. Because the PMT dynode signal is not periodic, we never exceed 2 GS/s.

When  $\mu^\pm$  decay occurs, the  $e^\pm$  is only *on average* delayed by  $\sim 2.2$  microseconds. As such, the oscilloscope should record a long enough waveform to capture the majority of decay events, without exceeding 2 GS/s and while keeping the size of the data manageable. We configured the oscilloscope as follows: the rising-edge trigger is positioned at 10% and set to a level of 300 mV. The vertical scaling is set to 500 mV/div. The horizontal scaling is set to 500 ns/div, recording 15,000 data points in 15 divisions for a total waveform length of 7.5  $\mu s$ . The Channel 1 input is used and impedance-matched at  $50\Omega$ . The oscilloscope is set in the ‘single-acquisition

mode'; whenever the trigger level is exceeded, the oscilloscope acquires the 15,000 point waveform record and stops sampling.

The LabVIEW program queries the oscilloscope on its acquisition state. If a waveform is acquired, it scans the record to determine the number of pulses; if it is not acquired, it simply waits another set period of time (1-2 seconds) before asking again.

The number of pulses is determined by specifying a scan interval ' $s$ ' (in nanoseconds) and some sensitivity threshold, ' $n$ ' (an integer). The program begins by calculating the mean  $m$  and standard deviation  $\sigma$  over the set of data points beginning with the very first data point, and with length equal to  $s$ . Thus, if  $s = 500$  ns, and we are sampling at 2 GS/s, it calculates  $m, \sigma$  over the first 1000 data points. If the *last* data point in this interval is not greater than  $m + n\sigma$ , it shifts over by one point and repeats the calculation. When some point at the end of  $s$  exceeds the threshold  $m + n\sigma$ , it is identified as a 'candidate point'. We used  $n = 5$  and  $s = 500$  ns, which prevents most of the voltage fluctuations from being read as candidates.

To prevent the scan from identifying every point on the rising edge of a pulse as a candidate, the program skips forward by a specified interval  $k$  immediately after a candidate is detected, and the process resumes until the scan interval reaches the end of the waveform record. We used  $k = 300$  ns.

If one candidate is detected, the program saves only the peak voltage of that pulse. If two candidates are found, it saves the entire waveform record, along with a 12-value preamble with relevant information.

### 3.3 Monte Carlo Method

Simulating the behavior of electrons and positrons is much more difficult than for heavier particles; because of their small mass,  $e^\pm$  are subject to more violent interactions and frequent changes in direction. An accurate simulation must keep track of the particle's location as it moves through the detector, losing energy to a number of interactions. For our purpose, it is impractical to model every interaction, as the large number of total interactions over macroscopic lengths would require enormous computing power. Instead, we impose a cutoff energy above which the energy loss processes are sampled discretely, and below which energy loss is simulated as a continuous process.

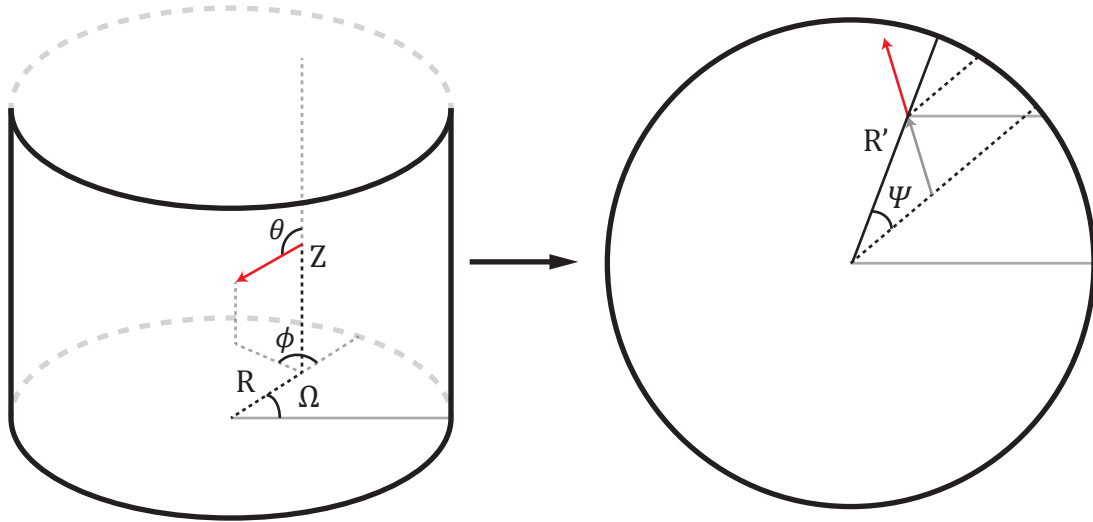


Figure 3.4: Global and local coordinate conventions in the Monte Carlo transport program.

### 3.3.1 Particle Tracking and Transport

The full Monte Carlo simulation is composed of a number of sub-modules which carry out specific functions on the  $e^\pm$ 's attributes. The motion of the  $e^\pm$  is simulated in discrete steps of a specified length  $s$ . After each transport step, the  $e^\pm$  is scattered into some new angle, which must be translated back to the global coordinates before being transported again.

A particle in the global coordinate system has a specified location  $\{R, Z, \Omega\}$  and, locally, an initial direction  $\{\theta, \phi\}$ . The polar coordinate,  $\theta$ , is always in reference to the cylindrical  $Z$ -axis, while  $\phi$  is in reference to the radial vector along  $R$ , as in Figure 3.4. We can see that moving the particle forward by  $s$  sends  $Z \rightarrow Z + s \cos \theta$ . From the law of cosines, the new radial coordinate  $R'$  is given by

$$R' = \sqrt{R^2 + s^2 \sin^2 \theta - 2Rs \sin \theta \cos(\pi - \phi)}, \quad (3.2)$$

and the phase offset  $\Psi$  is then

$$\Psi = \arccos \left[ \frac{R + s \sin \theta \cos \phi}{R'} \right]. \quad (3.3)$$

If  $(0 < \phi < \pi)$ , then we have  $\Omega \rightarrow \Omega + \Psi$  and  $\phi \rightarrow \phi - \Psi$ . Conversely, when  $(\pi < \phi < 2\pi)$ , then  $\Omega \rightarrow \Omega - \Psi$  and  $\phi \rightarrow \phi + \Psi$ . Of course,  $\theta$  is unchanged by particle transport.

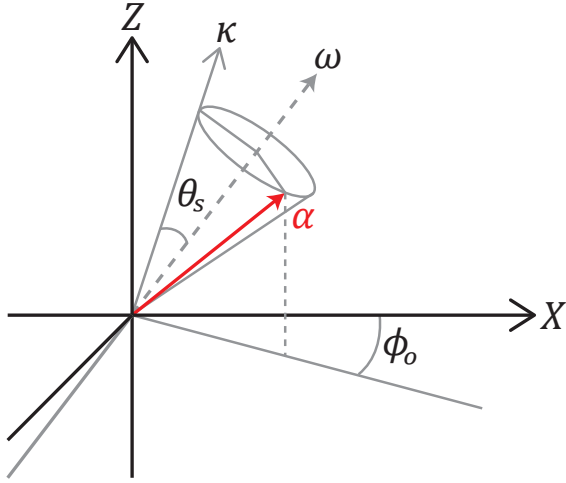


Figure 3.5: A particle with initial trajectory  $w$  is scattered at the origin by some angle  $\theta_s$ , and rotated by  $\phi_s$ . The new trajectory,  $\{\theta', \phi'\}$ , is determined by calculating the polar angle between  $Z$  and  $\alpha$ , and the azimuthal angle between  $X$  and the projection of  $\alpha$  into the  $X - Y$  plane.

After each step  $s$ , we scatter the particle into some new angle  $\theta_s$  inclined from its initial trajectory  $w$ . We always generate the azimuthal scattering angle  $\phi_s$  as a random number from 0 to  $2\pi$ , because the scattering cross-sections have cylindrical symmetry. In Figure 3.5, a particle with trajectory  $w$  is scattered into a cone of opening angle  $2\theta_s$  at the origin, and its final trajectory is  $\alpha$ . In this ‘scattering coordinate system’,  $\hat{x}, \hat{z}$ , and  $\omega$  are coplanar.

Using a rotation matrix, the vector  $\kappa = \{\sin(\theta - \theta_s), 0, \cos(\theta - \theta_s)\}$  is rotated through angle  $\phi_s$  about  $w$  to get  $\alpha$ . The vector angle between  $Z$  and  $\alpha$  is the particle’s new polar angle,  $\theta'$ . We then form the projection of the vector  $\alpha$  into the  $X - Y$  plane and calculate its angle from  $X$  to determine the offset angle,  $\phi_0$ . If  $(0 < \phi_s < \pi)$ , then the particle after scattering has new azimuthal angle  $\phi' = \phi - \phi_0$ , but if  $(\pi < \phi_s < 2\pi)$ , then the new coordinate is  $\phi' = \phi + \phi_0$ .

### 3.3.2 Hard Interactions

Above a specified kinetic energy  $T_{cut}$ , energy loss of  $e^\pm$  is simulated by the explicit production of secondary electrons from ionizing collisions. That is, these secondary electrons or ‘ $\delta$ -rays’ are only created with kinetic energy  $T > T_{cut}$ . By placing a limit on  $T$ , the mean free path between hard interactions is kept at a manageable scale, and we can sample these discrete events in a reasonable amount of computing time.

Recalling that the maximum kinetic energy transfer in  $e^-e^-$  scattering is  $E_k/2$ ,

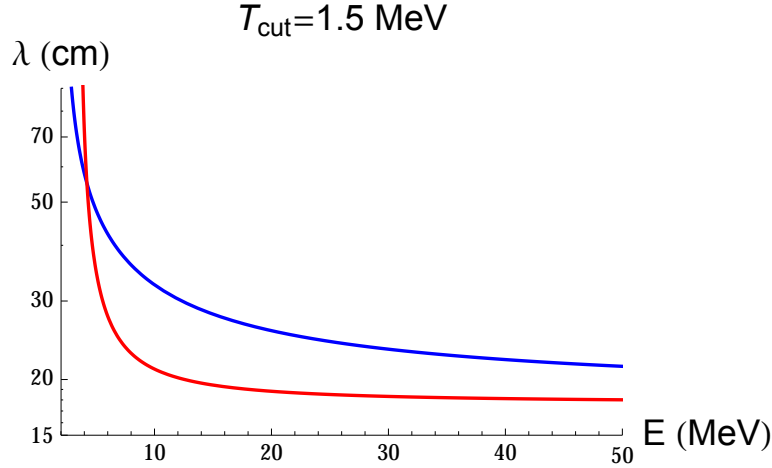


Figure 3.6: Mean free paths for the production of  $\delta$ -rays with  $T > T_{cut}$  by  $e^\pm$  with total energies from 2.011 - 50 MeV (positrons) and from 3.511-50 MeV (electrons). By imposing the limit  $T_{cut} = 1.5$  MeV, the mean free path is of the same length scale as the detector, and so the number of  $\delta$ -rays produced will not be too large.

then the incident electron must have kinetic energy  $E_k > 2T_{cut}$  to produce a  $\delta$ -ray. For positrons, the maximum transfer was  $E_k$ ; they must have kinetic energy  $E_k > T_{cut}$  to produce  $\delta$ -rays. For an incident electron with energy  $E$ , the total cross section per atom (of atomic number  $Z$ ) to produce a  $\delta$ -ray with kinetic energy  $T > T_{cut}$  is described by Møller ( $e^-e^-$ ) scattering[18],

$$\sigma_-(Z, E, T_{cut}) = \frac{2\pi r_e^2 Z}{\beta^2(\gamma - 1)} \times \left[ \frac{(\gamma - 1)^2}{\gamma^2} \left( \frac{1}{2} - x \right) + \frac{1}{x} - \frac{1}{1-x} - \frac{2\gamma - 1}{\gamma^2} \ln \left[ \frac{1-x}{x} \right] \right], \quad (3.4)$$

while for positrons, we use the Bhabha ( $e^+e^-$ ) scattering cross section,

$$\sigma_+(Z, E, T_{cut}) = \frac{2\pi r_e^2 Z}{(\gamma - 1)} \times \left[ \frac{1}{\beta^2} \left( \frac{1}{x} - 1 \right) + B_1 \ln x + B_2(1-x) - \frac{B_3}{2}(1-x^2) + \frac{B_4}{3}(1-x^3) \right], \quad (3.5)$$

with classical electron radius  $r_e$ , electron rest mass energy  $m_e$ , and

$$\begin{aligned}\beta &= v/c & \gamma &= E/m_e \\ x &= T_{cut}/(E - m_e) & y &= 1/(\gamma + 1) \\ B_1 &= 2 - y^2 & B_2 &= (1 - 2y)(3 + y^2) \\ B_3 &= (1 - 2y)^2 + (1 - 2y)^3 & B_4 &= (1 - 2y)^3.\end{aligned}$$

In our scintillator, the density of Hydrogen atoms is  $N_H = 5.17 \times 10^{22}$  atoms per  $\text{cm}^3$ , and the density of Carbon atoms is  $N_C = 4.69 \times 10^{22}$  atoms per  $\text{cm}^3$ . Therefore, the mean free path for these hard collisions is calculated by

$$\lambda_{\pm}(E, T_{cut}) = \left( \sum_i \left[ N_i \times \sigma_{\pm}(Z_i, E, T_{cut}) \right] \right)^{-1}. \quad (3.6)$$

The kinetic energy  $T$  of the produced  $\delta$ -ray is sampled from the differential cross sections per atom for Møller and Bhabha scattering. With  $\epsilon = T/(E - m_e)$ , where  $E$  is the energy of the incident electron, we have

$$\begin{aligned}\frac{d\sigma}{d\epsilon}(Z, E, T) = & \frac{2\pi r_e^2 Z}{\beta^2(\gamma - 1)} \times \\ & \left[ \frac{(\gamma - 1)^2}{\gamma^2} + \frac{1}{\epsilon} \left( \frac{1}{\epsilon} - \frac{2\gamma - 1}{\gamma^2} \right) + \frac{1}{1 - \epsilon} \left( \frac{1}{1 - \epsilon} - \frac{2\gamma - 1}{\gamma^2} \right) \right],\end{aligned} \quad (3.7)$$

and for an incident positron, we have

$$\frac{d\sigma}{d\epsilon}(Z, E, T) = \frac{2\pi r_e^2 Z}{(\gamma - 1)} \left[ \frac{1}{\beta^2 \epsilon^2} - \frac{B_1}{\epsilon} + B_2 - B_3 \epsilon + B_4 \epsilon^2 \right]. \quad (3.8)$$

As a practical matter, we first integrate the differential cross sections over the according kinematic limits ( $T_{cut} \leq T \leq E_k/2$  for  $e^-e^-$ , or  $T_{cut} \leq T \leq E_k$  for  $e^+e^-$ ) to get a normalization factor,  $N$ . Then, a value of  $T$  is sampled as a random variate from the normalized probability distribution

$$P(T) = \frac{1}{N} \left( N_H \frac{d\sigma}{d\epsilon}(1, E, T) + N_C \frac{d\sigma}{d\epsilon}(6, E, T) \right). \quad (3.9)$$

The initial particle is left with kinetic energy  $E_k - T$ . From conservation of



Figure 3.7: A particle of kinetic energy  $E_k$  and mass  $m$  transfers kinetic energy  $T$  to a particle with the same mass initially at rest. After collision, the incident particle is scattered by  $\theta_s$ , and the target particle is scattered by  $\theta_r$ .

momentum in the lab frame, in which the target electron is considered to be free and at rest<sup>1</sup> before the collision, we calculate the scattering angle of the incident particle  $\theta_s$  and the recoil angle of the target particle  $\theta_r$ , as in Figure 3.7, by

$$\begin{aligned}\theta_s &= \arccos \left[ \frac{p_\delta^2 - p_i^2 - p_f^2}{-2p_i p_f} \right], \\ \theta_r &= \arctan \left[ \frac{p_f \sin \theta_s}{p_i - p_f \cos \theta_s} \right],\end{aligned}\quad (3.10)$$

where  $p_\delta$ ,  $p_i$ , and  $p_f$  are the relativistic 3-momenta of the  $\delta$ -ray, the initial  $e^\pm$ , and the final  $e^\pm$ , respectively. As before, the azimuthal scattering angle  $\phi_s$  is generated isotropically, with the condition that the  $\delta$ -ray be scattered into  $\phi_s - \pi$ , i.e., in the opposite direction from the final  $e^\pm$ .

### 3.3.3 Soft Interactions

The non-catastrophic or ‘soft’ interactions are those with low-energy-transfer occurring frequently enough to be viewed as “statistically grouped” interactions. Primarily, we have low-energy Møller and Bhabha scattering, atomic excitation, bremsstrahlung, and elastic scattering from nuclei.

The Landau-Vavilov distribution describes the cumulative effects of collisional energy losses due to Møller/Bhabha scattering and atomic excitation. We use the Particle Data Group’s parametrization[10] for the most probable energy loss,

$$\Delta_p(x) = \xi(x) \times \left[ \ln \frac{2m_e \beta^2 \gamma^2}{I} + \ln \frac{\xi}{I} + j - \beta^2 - \delta \right], \quad (3.11)$$

<sup>1</sup>We ignore the nuclear binding energy, which is valid if  $T_{cut} \gg I$ , the mean excitation potential of the material.

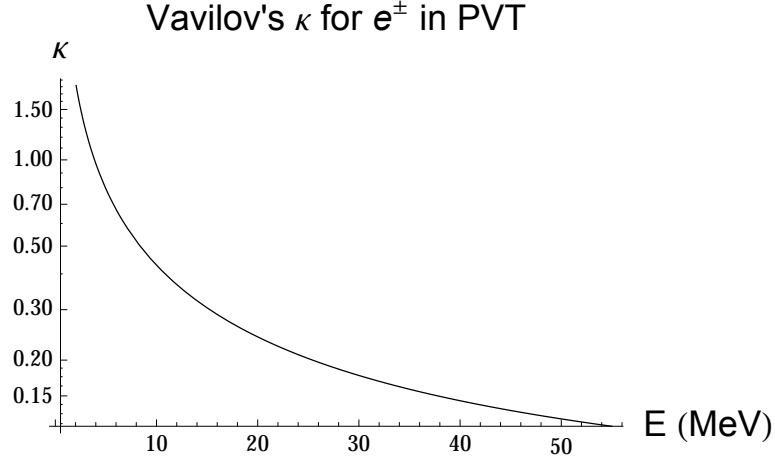


Figure 3.8: Plot of Vavilov's  $\kappa$  parameter for  $e^\pm$  traveling in PVT-based scintillator. Because  $\kappa < 10$  for energies in the range .511 – 55 MeV, we use the Landau-Vavilov most probable energy loss, rather than the Bethe-Bloch mean energy loss.

with

$$\xi(x) = \frac{K}{2} \left\langle \frac{Z}{A} \right\rangle \frac{x}{\beta^2}, \quad (3.12)$$

where  $K = .307075$  MeV mol $^{-1}$  cm $^2$ ,  $j = .2$ ,  $x = s\rho$  is the thickness of the path length  $s$  in g cm $^{-2}$ ,  $I$  is the mean excitation potential, and  $\delta$  is the Bethe-Bloch density correction. In Figure 3.8, we see that the Vavilov parameter  $\kappa$  is less than 10 for  $e^\pm$  energies from .511-55 MeV. This tells us that the continuous collisional energy loss over a step  $s$  should indeed be calculated from  $\Delta_p(x)$ .

We approximate the continuous energy loss due to bremsstrahlung from the radiative stopping powers tabulated in the NIST Estar database. Because the step length  $s = .2$  cm is small, the radiative energy loss per unit path length does not vary significantly over a single step. Thus, in a step of  $s = .2$  cm, the energy loss due to bremsstrahlung is

$$\Delta E_{rad} \simeq -.2 \left( \frac{dE}{dx} \right)_{rad}. \quad (3.13)$$

At higher energies, the radiative losses would begin to dominate energy loss, and we would need to treat them in a similar way as the explicit  $\delta$ -ray production. Below the critical energy  $E_c$ , however, collisional energy losses are dominant, and the NIST Estar data is an accurate approximation.

The elastic scattering of  $e^\pm$  by atomic nuclei is treated in the multiple scattering formalism of Molière[19]. The individual scattering of  $e^\pm$  is predominantly small angle, and the composition of many ( $n > 20$ ) scattering events over a path  $s$  is approximately Gaussian for the central 98% of the angular distribution[10]. The rms

angular deflection, after traveling  $s$  cm, is given by

$$\theta_{rms} = \frac{13.6 \text{ MeV}}{v p} \sqrt{s/X_0} \left[ 1 + .038 \ln(s/X_0) \right], \quad (3.14)$$

where  $v$  and  $p$  are the velocity and momentum of the incident  $e^\pm$ , and  $X_0$  is the radiation length in PVT, 42.54 cm.

### 3.3.4 Simulation Logic

The full simulation takes five inputs: number of events  $N_{sim}$ , muon rest energy  $m_\mu$ , energy cutoff  $E_{cut}$ , production threshold  $T_{cut}$ , and step length  $s$ . An event is generated by randomly assigning a location  $\{R, Z\}$  with  $R < 10$  cm and  $Z < 40$  cm, a charge  $C = 1$  or  $-1$ , and an energy  $m_e < E_e < (m_\mu^2 + m_e^2)/2m_\mu$ .

The trajectory  $\{\theta, \phi\}$  is sampled by generating three random numbers  $X, Y, Z$ , each from the interval  $[-1, 1]$ . If  $R = \sqrt{X^2 + Y^2 + Z^2} \leq 1$ , then  $\theta$  is taken to be the polar angle of the vector  $\{X, Y, Z\}$  in spherical coordinates, and  $\phi$  is the angle between the projection  $\{X, Y, 0\}$  and the  $X$ -axis, running from 0 to  $2\pi$ .

We name variables  $L = 0$ ,  $E_k = E_e - m_e$ , and  $E_d = 0$  to keep track of the particle's traveled distance, remaining kinetic energy, and total deposited energy in the detector. At the beginning of the simulation and after each transport step, we check if  $E_k > E_{cut}$ . If  $E_k < E_{cut}$ , then the particle is ‘terminated’, and we set its kinetic energy to  $E_k = 0$  while  $E_d \rightarrow E_d + E_k$ ; it deposits all of its remaining kinetic energy to the detector.

If we have  $E_k > E_{cut}$  to begin with, then the program calculates  $\lambda_\pm(E_k + m_e, T_{cut})$ , the distance  $e^\pm$  must travel before a hard collision occurs. We transport the particle from  $\{R, Z, \Omega\} \rightarrow \{R', Z', \Omega'\}$  by step length  $s$ , and if  $R' < 10$  and  $0 < Z' < 40$ , we then calculate the collisional and radiative energy losses from (3.11) and (3.13), subtract them from  $E_k$ , and add them to  $E_d$ . We set  $L \rightarrow L + s$  and calculate the deflection angle  $\theta_{rms}$  due to multiple elastic scattering from nuclei from (3.14). The particle's trajectory is then transformed from  $\{\theta, \phi\} \rightarrow \{\theta', \phi'\}$  using the geometric procedure outlined earlier, and we are ready to repeat the transport procedure.

If a transport step takes a particle outside of the detector boundary, i.e.  $R' > 10$ ,  $Z' < 0$ , or  $Z' > 40$ , then we calculate its energy loss over a distance  $s/2$ , add this to  $E_d$ , and terminate the particle's history by setting  $E_k = 0$ .

Whenever the traveled distance  $L$  exceeds  $\lambda_\pm$ , we generate a secondary electron by sampling its kinetic energy  $T$  as previously described. The primary particle's kinetic energy is then set to  $E_k \rightarrow E_k - T$ , and the path length to the next hard collision is

re-calculated at energy  $E_k - T + m_e$ , while  $L$  is set to 0. No change is made to  $E_d$ .

The scattering angles of the primary and secondary particles,  $\theta_s$  and  $\theta_r$ , are calculated by (3.10) and their trajectories are transformed to  $\{\theta', \phi'\}$ . The location, trajectory, and kinetic energy of the secondary particle is saved, and the primary particle continues to be transported and transformed until it either deposits all of its kinetic energy or escapes the detector. Each secondary particle is then transported and transformed just as if it were a primary particle, and the total energy deposition is then  $E_d = E_d^p + E_d^1 + E_d^2 + \dots + E_d^n$ , where  $n$  is the number of secondary particles created by the primary,  $p$ . As a last step, we simulate positron annihilation  $e^+e^- \rightarrow \gamma\gamma$  by adding  $2m_e$  to  $E_d$  whenever a positron reaches  $E_k < E_{cut}$ , in addition to whatever residual kinetic energy it deposits in the detector.

In Figure 3.9, we see that the electrons traveling through matter follow a tortuous path as they lose energy to soft collisions, bremsstrahlung, and the generation of  $\delta$ -rays. We can imagine, then, that high-energy  $e^\pm$  produced in muon decays should be even more susceptible to electron escape, as they produce more secondary particles and are deflected from their path more often than low-energy  $e^\pm$ , providing more instances for energy to be carried out of the detector.

Every event has a ‘true’ energy  $E_e$  that we sampled randomly, and an ‘apparent’ or deposited energy,  $E_d$ . After calculating  $E_d$ , we assign each event a ‘probability factor’ of  $Q = R \times P(E_e)$ , where  $P(E_e)$  is the probability that an  $e^\pm$  be produced with energy  $E_e$  in  $\mu^\pm$  decay, from Chapter 1.  $R$  is simply the initial radial coordinate, which is applied to account for the fact that the differential volume within the detector at radius  $R$  scales by a factor of  $R$ . The probability factor  $Q$  is where we recover the underlying physics of muon decay, by preferentially weighting events in the high-energy end of the spectrum as predicted by the Fermi distribution.

An energy distribution is formed from a large set of  $\{E_d, Q\}$  events. Because the simulated and experimental data use different metrics for measuring  $E_e$ , all distributions are normalized to their highest energy value; for a set of simulated events, each  $E_d^i$  is divided by the maximum  $E_d^{max}$  of the set. We specify a binning number,  $n$ , and group events into evenly-spaced increments of width  $1/n$ . The  $Q$  factors are summed in each bin, and finally, we normalize the sum of all  $Q$ ’s to equal the number of data points in the experimental distribution.

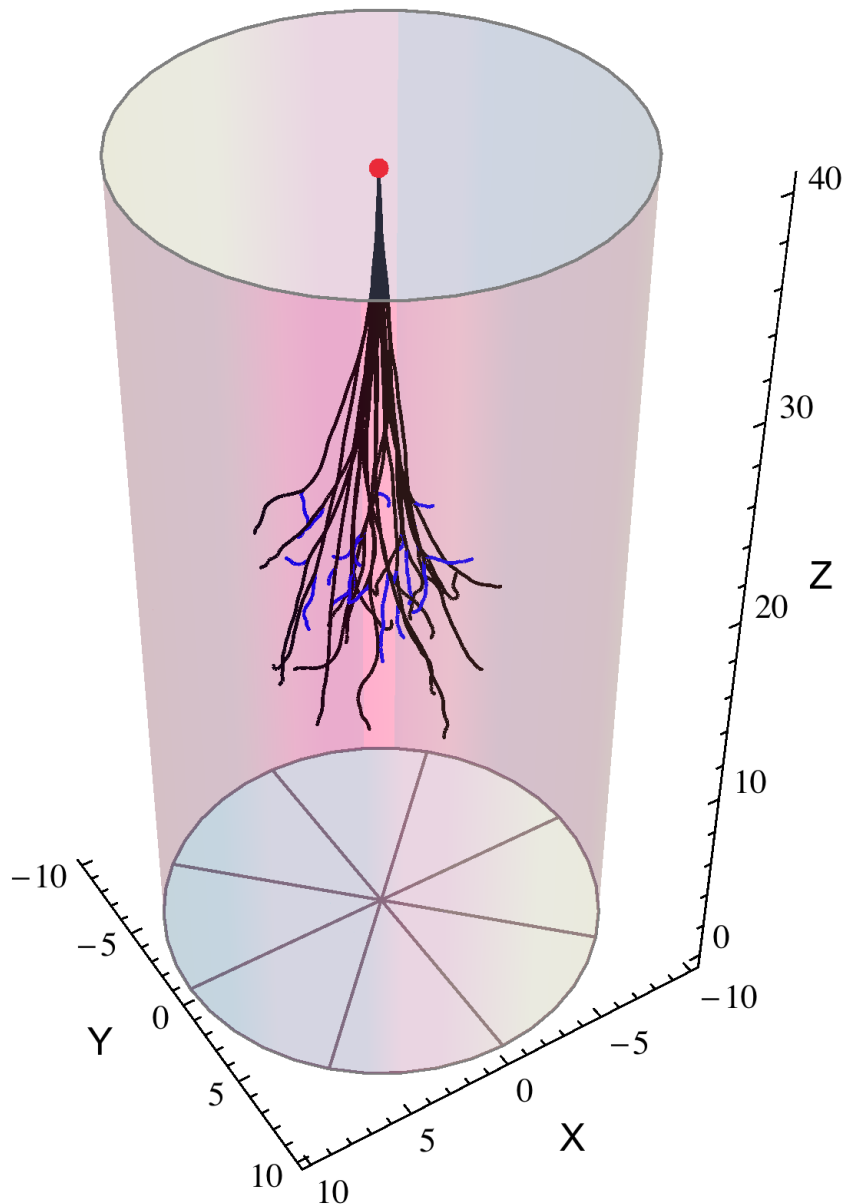


Figure 3.9: Simulated particle tracks for 20 electrons with the same initial configuration, starting from the red dot at  $\{0, 39\}$  with trajectory  $\{\pi, 0\}$  and total energy 50.511 MeV. Primary electron paths are colored in black, while  $\delta$ -ray paths are colored in blue. For this simulation,  $E_{cut} = .5$  MeV,  $T_{cut} = 1.5$  MeV, and  $s = .2$  cm. Every simulated particle deposited its available 50 MeV within the detector.

# Chapter 4

## Results and Analysis

Data were collected daily from 2/12/2015 to 4/15/2015 with the PMT powered at 1200 V and 1000 V for roughly equal periods of collection time. At 1200 V, one-pulse events were only recorded after 2/28/2015, with a total 565620 one-pulse events recorded. In the same period of time, 4163 two-pulse events were recorded. Therefore, approximately one event in 137 is a two-pulse event. In total, 6309 two-pulse events were recorded at 1200 V, and 4303 two-pulse events were recorded at 1000 V. We also recorded 628124 one-pulse events at 1000 V.

All events were recorded with the same configurations as detailed in Chapter 3, except for the difference in supplied voltage of the PMT. Each two-pulse data record is structured as

$$\{N_p, \text{dt}, V_{pk}, i_{pk}, \Delta t, m_1, \sigma_1, m_2, \sigma_2, i_1, i_2, s, (\text{waveform data})\} ,$$

where  $N_p$  is the number of points in (waveform data),  $\text{dt}$  is the time per point,  $V_{pk}$  is the peak voltage of the second pulse,  $i_{pk}$  is the offset index of this peak from the second candidate point, and  $\Delta t$  is the time elapsed between first and second candidates.  $m_n$  and  $\sigma_n$  are the mean and standard deviation preceding the  $n$ th candidate point, and  $i_n$  is its index in (waveform data).  $s$  is the scan length in number of data points. Waveform data is simply the voltage values of each of the data points in the record.

### 4.1 Pulse Processing & Integration

The data must first be processed and integrated to constitute a ‘measurement’ of  $E_{e^\pm}$ . First, we throw out any events where  $\Delta t < t_{cut}$  for a specified value of  $t_{cut}$ . We want to avoid two-pulse events where the  $e^\pm$  signal occurs too soon after the  $\mu^\pm$ ’s,

because the delayed component of the first signal may be ‘buried’ underneath the second signal, thus raising it artificially. We used  $t_{cut} = 1.0 \times 10^{-6}$  s, which appears to be long enough for the  $\mu^\pm$  signal to decay completely. As  $E_{e^\pm}$  is not correlated with the muon lifetime  $\tau_\mu$ , removing events by  $\Delta t < t_{cut}$  does not bias the remaining data. This step cuts 1095 events from the 1200V-data and 863 from the 1000V-data.

Next, we clip off the waveform data preceding  $i_2$ , as we are only interested in the second signal. We subtract  $m_2$  from the remaining data points in order to remove any ‘baseline’ voltage preceding the signal, as again, we are only interested in the change in voltage due to the passage of an  $e^\pm$  through the detector.

While the LabVIEW program finds the candidate start point,  $i_2$ , we now need to choose the ‘endpoint’ of our integration, where the second pulse has effectively reached zero. Similar to before, we specify an integer  $n_f$ , and test each point (to the right of the peak,  $i_{pk}$ ) to see if it has fallen below  $n_f \sigma_2$ . If we reach the end of the waveform without finding such a point, then the signal was clipped at the end of the oscilloscope’s acquisition before it could relax to zero. These events are thrown out from the remaining data, and the waveforms are clipped off past the determined endpoint.

We add another stage of amplitude discrimination to remove ‘blip’ events and very weak signals. Blips occur when a single point jumps above  $5 \sigma_2$  due to noise in the PMT signal, thus registering as a second pulse. If, in the remaining waveform, no data points exceed  $n_{cut} \sigma_2$ , then the event is thrown out. We used  $n_{cut} = 6$  to ensure that all data points have at least some ‘rising’ and ‘falling’ shape. This cuts another 924 events from the 1200V-data and 154 events from the 1000V-data.

Finally, we generate an interpolating function for each waveform, and integrate the area under the resulting curve in Mathematica. We normalize these ‘energies’ to the maximum value of the set, then bin the data to produce an experimental distribution.

## 4.2 Energy Distributions

The experimental energy distributions are plotted in Figure 4.1. Here,  $\chi$  is split into 30 bins. The two distributions differ most significantly in the low-energy regime. In the 1200 V-data, the first two bins contain 1139 events, just over 1/4 of all plotted events. By comparison, the 1000 V-data contains 374 events in its lowest two bins, or  $\sim 1/10$  of all plotted events. This discrepancy can be understood as due to higher inter-dynode voltage differences when the PMT is operated at 1200 V as opposed to 1000 V. We also see that a very small number of exceptionally high-energy events,

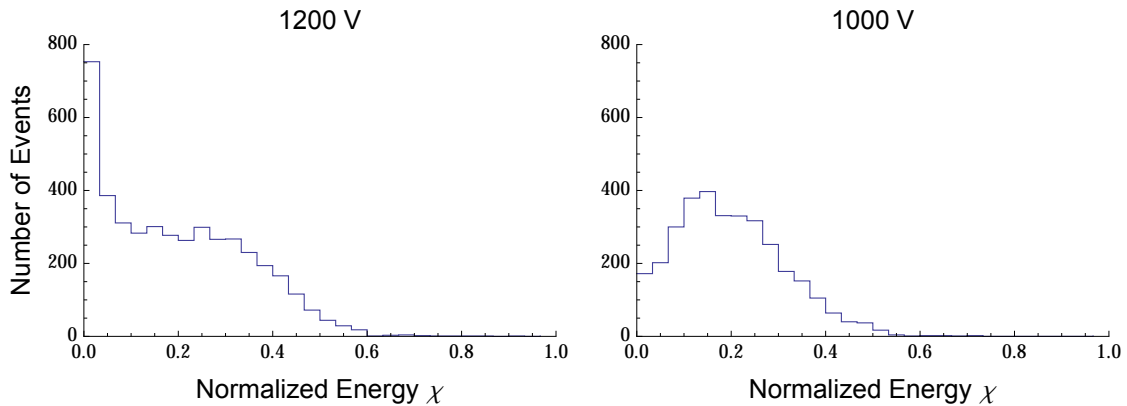


Figure 4.1: Experimental distributions of normalized  $e^\pm$  energy,  $\chi$ . There are 4291 events in the set collected with the PMT operating at 1200V, and 3286 events from the set collected at 1000V. Both distributions have 30 bins.

from  $\chi = .6$  up to  $\chi = 1$ , have skewed the distribution to lower energies. These are likely due to the rare coincidence of two  $\mu^\pm$  entering the scintillator within  $6.75 \times 10^{-6}$  s of each other.

### 4.2.1 Weak Pulses

When the PMT is powered at higher voltages, the inter-dynode potential differences increase. Consequently,  $\delta$  at each dynode is increased, as well as the overall gain factor  $g$ . Thus, when operated at 1200 V, weak scintillations and thermionic emissions are more likely to produce greater numbers of secondary electrons at the first dynode, and a stronger overall pulse. Because these low-energy events are more strongly amplified in the 1200 V setting, they more often exceed the  $5\sigma_2$  threshold, and therefore we see a greater number of low-energy pulses than in the 1000 V-data.

To understand these low-energy events, we look at the first 1500 events of the 1200 V-data, which corresponds to the first three bins in Figure 4.1. This subset is re-normalized and plotted in Figure 4.2, where we see the same distinct peaks corresponding to 1,2, and 3 incident photoelectrons.

To prevent this artifact being compared with the simulated distributions, we cut the 543 lowest-energy events corresponding to the first three bins in Figure 4.2, which approximately represents the spread of single-photoelectron events. In doing so, we have removed the “true” single-photoelectron events, due to  $e^\pm$  scintillation, along with the unknown number of thermionic emissions. However, we can be sure that this does not affect the overall distribution by comparing the relative sizes of the integrated

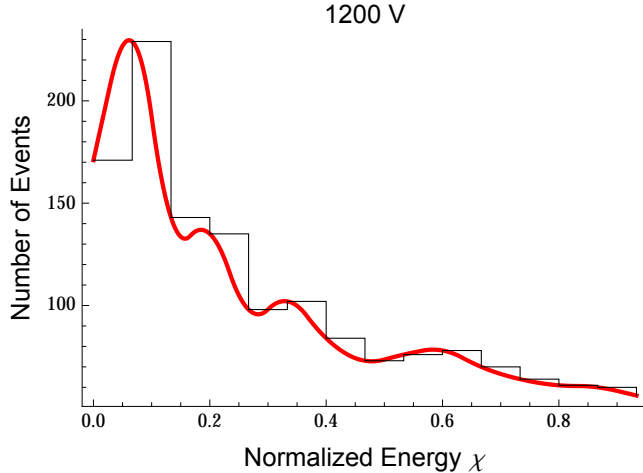


Figure 4.2: Renormalized distribution of the 1500 lowest-energy events from the 1200V-data, in 15 bins (black) and with an interpolation of the distribution overlaid (red). We can distinguish the characteristic peaks of 1,2, and 3-photoelectron events, for which the statistical broadening of  $\delta$  at the first dynode is small, as described in Chapter 2.

pulses. After cutting the single-photoelectron events, the lowest integrated pulse value is 10.8882, while the highest non-outlying pulse is  $\sim 333$ ; we have removed  $\sim 3\%$  of the energy range in this cut.

### 4.2.2 High-energy Anomalies

In the raw data, we see a sharp drop off in the number of events above  $\chi \simeq .6$ . In the 1200 V-data, the first 18 bins contain 4275 events; the remaining 12 bins contain only 16 events, or  $\sim 3.7\%$  of the entire set. Likewise, for the 1000 V-data, the 14 highest bins contain just 13 events, or  $\sim 3.9\%$  of the whole set.

These exceptionally high-energy events are likely due to the rare occurrence of two particles crossing the detector within  $\sim 6.75 \times 10^{-6}$  seconds of each other. These particles can be either charged, such as electrons or muons, or neutral, such as photons or neutrons, which may produce charged particles by interacting with atoms in the scintillator.

We can convince ourselves that these high-energy outliers are due to some other particles by considering what we know about  $\mu^\pm$  decay; that high-energy  $e^\pm$  are more likely to be emitted than low-energy  $e^\pm$ , and that even the highest energy  $e^\pm$ , at  $\sim 55$  MeV, are capable of depositing all of their energy without escaping the detector. Thus, it would be highly improbable for just 15  $e^\pm$  to deposit energies in the range of 33-55 MeV ( $.6\text{-}1 \chi$ ), while the other 4276  $e^\pm$  deposited less than 33 MeV in the

detector. Such a sharp cutoff is not predicted either by the  $P(E_{e^\pm})$  distribution or the geometric properties of the detector; it must be due to some other source of particles.

To strengthen this assertion, we can consider the probability of observing two  $\mu^\pm$  crossing the detector in  $6.75 \times 10^{-6}$  s, given that  $\mu^\pm$  cross the detector at an average rate  $r$ . As the crossing of a  $\mu^\pm$  occurs independently of the time since the previous crossing, the statistics follow a Poisson distribution.

If an average number  $\lambda$  of muons cross the detector in a time interval  $\Delta t$ , then the probability of observing exactly  $\nu$  events in  $\Delta t$  is

$$P_\lambda(\nu) = \frac{\lambda^\nu}{\nu!} e^{-\lambda}. \quad (4.1)$$

The muon flux rate at sea level exhibits a cosine-squared dependence on polar angle, often approximated by[20]

$$I(\theta) = I_v \cos^2 \theta, \quad (4.2)$$

where  $I_v = 0.006 \text{ cm}^{-2} \text{ s}^{-1} \text{ sr}^{-1}$ . Therefore, the number of muons originating from within solid angle  $d\Omega$  and passing through the differential area  $dA$  in time  $dt$  is

$$dN = I(\theta) d\Omega dA dt. \quad (4.3)$$

Through the top of the cylinder, we have

$$\begin{aligned} \int dN &= \int I(\theta) d\Omega dA dt \\ &= \int_0^{\pi/2} I_v \sin \theta \cos^2 \theta d\theta \int_0^{2\pi} d\phi \int dA \int dt, \end{aligned} \quad (4.4)$$

where we integrate  $\theta$  from 0 to  $\pi/2$ , as the muons must originate from above the horizon. From  $\int dA = \pi R^2$ , where  $R = 10 \text{ cm}$ , then the rate of muons is given by

$$R_1 = \frac{N}{\Delta t} = \frac{2}{3} I_v (\pi R)^2 \approx 4 \text{ s}^{-1}. \quad (4.5)$$

We also have muons passing through the sides of the cylinder, where  $\int dA = 2\pi R H$  with  $H = 40 \text{ cm}$ . This time,  $\phi$  is integrated only from 0 to  $\pi$  to count only those

muons crossing *into* the detector from the outside:

$$R_2 = \int_0^{\pi/2} \sin \theta \cos^2 \theta d\theta \int_0^\pi d\phi \int dA \\ \approx 16 \text{ s}^{-1}. \quad (4.6)$$

Now, the total rate of crossing events is  $r \approx 20 \text{ s}^{-1}$ . We are interested in the conditional probability of observing a muon in  $6.75 \times 10^{-6} \text{ s}$ , given that one was observed in  $7.5 \times 10^{-6} \text{ s}$ . The conditional probability of  $A$  given  $B$  is defined as

$$P(A|B) = \frac{P(A \cap B)}{P(B)} \quad (4.7)$$

where  $A \cap B$  is the intersection of events  $A$  and  $B$ ; for our problem, this is the probability of two muons being observed in a period of  $6.75 \times 10^{-6} \text{ s}$ .

Therefore, the probability of two-muon coincidence is

$$P_c = \frac{(6.75 r \times 10^{-6})^2}{2(7.5 r \times 10^{-6})} e^{r(7.5 - 6.75) \times 10^{-6}} \approx 6 \times 10^{-5}. \quad (4.8)$$

We can now estimate how many two-pulse events were due to muon coincidence by multiplying  $P_c$  by the total number of observations taken. At 1200 V, we observed approximately<sup>1</sup> 864333 total events, and so we might expect to have  $\sim 51$  muon coincidence events. At 1000 V, we made 632427 total observations, which would predict  $\sim 38$  muon coincidence events.

While we observed 16 high-energy events in the highest 12 bins of the 1200 V-data, there are likely additional events due to muon coincidence distributed throughout the other 18 bins, mixed in with the  $\mu^\pm$  decay events. Thus, there may be  $\sim 40$  muon coincidence events in the 1200 V-data, which is near that as predicted by our Poisson counting approximation. For the 1000 V-data, the 13 highest-energy events were found in the highest 14 bins; by extrapolation, then, there may be  $\sim 28$  muon coincidence events in all 30 bins, which again is close to the predicted value.

---

<sup>1</sup>Because muon data wasn't recorded for some of the earlier runs, we estimate the number of total observations by multiplying the number two-pulse events, 6309, by the average ratio of total events to two-pulse events, 137.

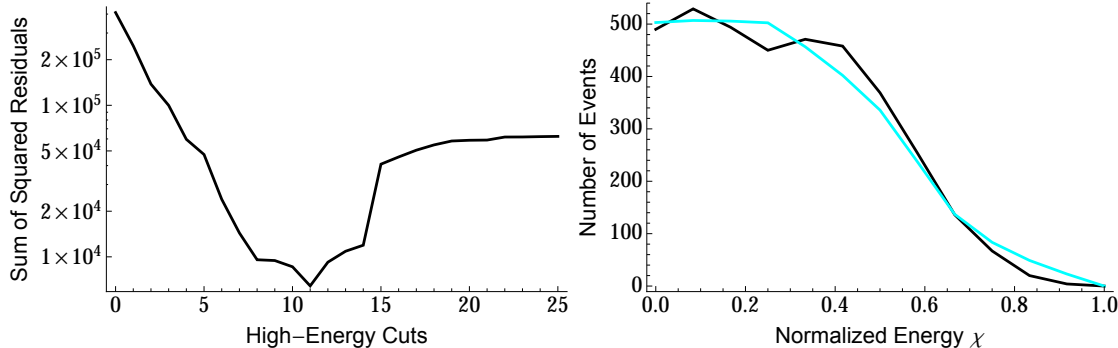


Figure 4.3: Sum of squared residuals between the  $m_\mu = 105$  simulated distribution and the experimental distribution with increasing cuts to the high-energy range (Left), and plots of the closest agreement between experimental and simulated distributions, when  $n_{cuts} = 11$  (Right). The experimental distribution is plotted in Black, and the simulated distribution is plotted in Cyan. The simulated distribution is generated from 100000 events, and normalized to the size of the experimental distribution after high-range cuts.

### 4.3 Measurement of $m_\mu$

Having cut the 543 lowest-energy events, we must now determine the appropriate number of cuts to the high-energy end of the 1200 V distribution. We do this by generating a simulated distribution at  $m_\mu = 105$  MeV, and comparing it to the experimental distribution as we sequentially cut more and more high-energy events. Specifically, the simulated and experimental distributions are binned at the same value, and we quantify their variance by calculating the sum of the squared residuals over all of their bins. We reduce the number of bins from 30 to 12 for a smoother experimental distribution.

On the left side of Figure 4.3, we see that cutting the 11 highest-energy events from the data produces the closest agreement with the simulated distribution. On the right side, the resulting experimental distribution is plotted with that of the  $m_\mu = 105$  MeV simulation. We are left with a remaining 3737 events in the experimental distribution.

To measure  $m_\mu$ , we generated simulated distributions at values of  $m_\mu = 90, 95, 100, 105, 110, 115$ , and  $120$  MeV. Each simulated distribution is generated from 100000 events, then scaled down to represent 3737 events, and the energies are normalized to 1.

The simulated distributions are shown in comparison with the experimental distribution on the left of Figure 4.4, with the various colors representing different as-

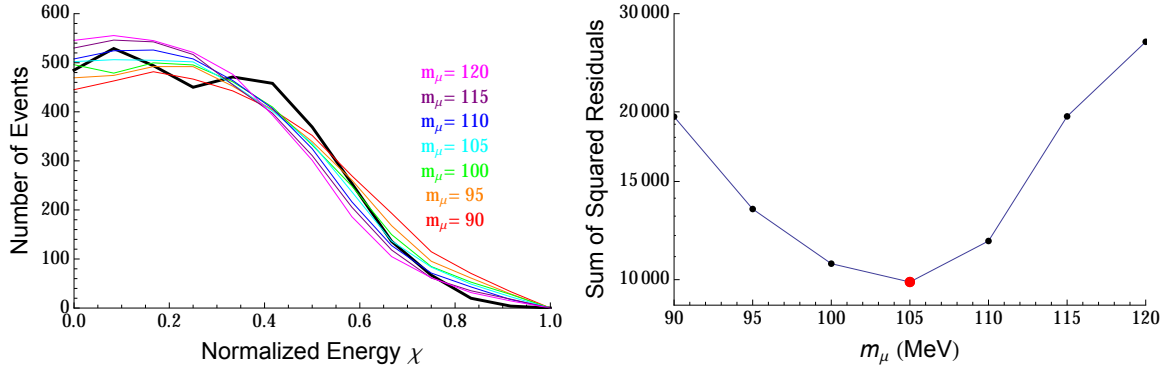


Figure 4.4: Left: Experimental distribution of normalized energy  $\chi$  from 1200V-data (Black) plotted with simulated distributions assuming different values for  $m_\mu$  (Color). Right: The sum of squared residuals between the experimental distribution and simulated distributions at different values of  $m_\mu$ . We see that  $m_\mu = 105$  MeV produces the strongest agreement (minimum residuals) between observed and simulated results, in agreement with the known value  $m_\mu = 105.6583715 \pm 0.0000035$  MeV[21].

sumptions of the value of  $m_\mu$ . On the right of Figure 4.4, the sum of squared residuals between each simulated distribution and the experimental distribution are plotted as a function of  $m_\mu$ . We see that, at  $m_\mu = 105$  MeV, the experimental and simulated distributions are in closest agreement. This tells us that the correct value of  $m_\mu$  is indeed 105 MeV.

We repeat the procedure in much the same way for the 1000 V-data. However, due to the drop off in low-energy events resulting from the lowered gain, we can only draw meaningful comparisons to simulated distributions above some threshold  $\chi$ . We make no low-energy cuts, since we cannot reliably determine which events are single-photoelectron events. Instead, we make our comparison over *only the 9 highest bins* of both distributions, to work around the drop off imposed by the  $5\sigma_2$  threshold. Again, we reduce the binning from 30 to 12 for a smoother experimental distribution.

The simulated distributions are normalized such that the sum of events over the 9 highest-energy bins equals the same sum for the experimental distribution. By this procedure, we find that 14 high-energy cuts produces the best agreement over the 9 highest bins.

In the left side of Figure 4.5, the 1000 V experimental distribution is plotted with simulations at the same values of  $m_\mu$  as before. The dotted vertical line represents the threshold  $\chi$ , above which the comparisons are made. On the right side of Figure 4.5, we see that the sum of squared residuals between simulated and experimental distributions is again minimized when  $m_\mu = 105$  MeV. The Monte Carlo simulation has proven to be an accurate model for energy deposition in a scintillating detector.

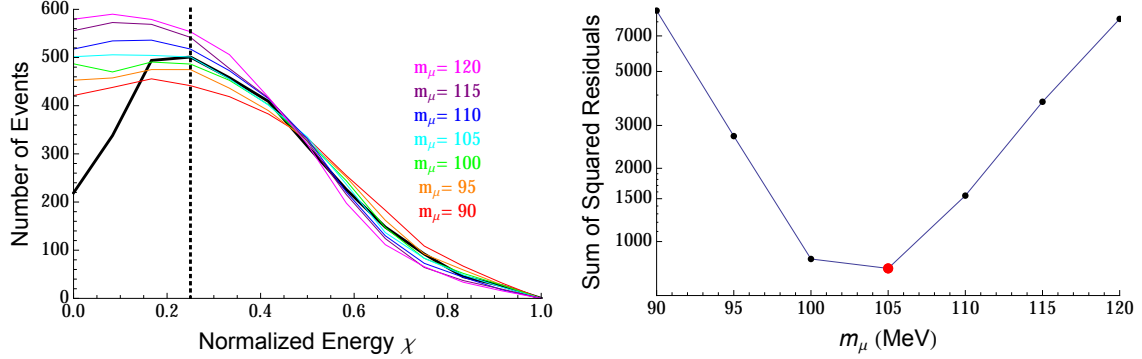


Figure 4.5: Left: Experimental energy distribution from 1000V-data (Black) plotted with simulated distributions at different values of  $m_\mu$  (Color). The vertical dotted line represents the threshold  $\chi$ , above which we calculate the residuals. Right: The sum of squared residuals over the 9 highest bins between experimental and simulated distributions.  $m_\mu = 105$  MeV produces the strongest agreement between observed and simulated results, and supports the same finding from the 1200V-data.

## 4.4 Measurement of $\tau_\mu$

Lastly, we can repeat the muon lifetime experiment by looking at the distribution of decay times  $\Delta t$  separating the two candidate signals. If we begin with a population of  $N_0$  muons at time  $t = 0$ , then we expect to have

$$N(t) = N_0 e^{-\Gamma t} \quad (4.9)$$

muons remaining at a later time  $t$ , where  $\Gamma \equiv 1/\tau_\mu$ . For this purpose, we want as little contribution from background events as possible, to avoid skewing the distribution over  $\Delta t$ . Using just the 1000 V-data, we generate a histogram of the decay times  $\Delta t$ , and fit this to a generic function  $F(t) = Ae^{-Bt}$  as depicted in Figure 4.6. Finding that  $A = 532$  and  $B = 455909$ , this tells us that  $\tau_\mu = 1/B \approx 2.193 \times 10^{-6}$  s, in close agreement with the accepted value of  $\tau_\mu = 2.197 \mu\text{s}$ .

Of course, the range of observed  $\Delta t$  is cut off below  $\sim 3 \times 10^{-6}$  and above  $6.75 \times 10^{-6}$ , corresponding to the skip interval  $k$  and the cutoff of the oscilloscope's acquisition, respectively. It is likely that recording more events over a longer interval  $\Delta t$  would produce a more accurate measurement of  $\tau_\mu$ , but this would come at the expense of resolving the area under the pulses necessary for quantifying their energy.

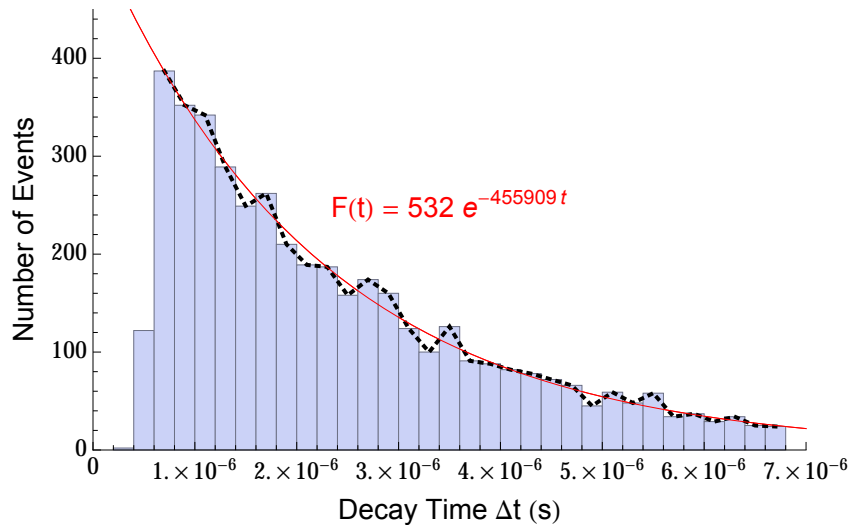


Figure 4.6: Histogram of decay times  $\Delta t$  separating candidate signals of two-pulse events in the 1000V-data. Fitting this histogram to an exponential function (Red) gives us that the observed muon lifetime is  $\tau_\mu \approx 2.193 \times 10^{-6}$  s.

# Conclusion

We began by studying the three-body decay of the muon, where we saw that the emitted electron (or positron) can be produced with a range of energies,  $P(E_{e^\pm})$ . Next, we saw that the  $e^\pm$ s deposit their energy, in the form of collisional and radiative losses, as they traverse matter, and that this energy is rapidly converted into an electronic signal by the scintillation detector. Assuming the amplification of scintillation pulses to be linear, we asserted that the relative integrated areas under pulses constitutes a measurement of the relative energies deposited by each of the  $e^\pm$ . By observing a large number of muon decays, we normalized the distribution of  $e^\pm$  energies in order to compare it with simulated distributions generated by a Monte Carlo method. We have found that a simulated value of  $m_\mu = 105$  MeV most closely matches the observed distribution, and is thus the true value of  $m_\mu$ . We also saw that the observed distribution of decay times exhibited the characteristic muon lifetime,  $\tau_\mu \approx 2.2\ \mu\text{s}$ .

The goal of this thesis was to demonstrate that large-volume scintillation detectors, commonly used to measure  $\tau_\mu$ , may be adapted to measure  $m_\mu$  by using a fast digitizing oscilloscope. The accuracy of this measurement may be increased on two fronts: through collecting a larger sample of data, and through improvements to the Monte Carlo simulation.

Although we had a limited window of operational time, we collected enough events to claim a measurement of  $m_\mu$ . With a greater number of events, we might begin to see nuances in the shape of the experimental distributions that are not accounted for by the simulation. Some areas of improvement would include the addition of more hard interactions, such as large-angle single elastic scattering from nuclei, in-flight positron annihilation, and hard bremsstrahlung emission. However, these would ultimately necessitate a new branch of code for the transport and interaction of photons, which is dominated at lower energies by Compton scattering. A model this complete would require significantly longer computation times to produce simulated distributions; our approximate model sufficiently describes the physics of energy loss by  $e^\pm$  in a scintillating detector.



# References

- [1] A discovery of cosmic proportions. *CERN Courier*, July 2012.
- [2] J. J. Beatty, J. Matthews, and S. P. Wakely. *Cosmic Rays*. Particle Data Group, October 2013.
- [3] Bradley W. Carroll and Dale A. Ostlie. *An Introduction to Modern Astrophysics*. Addison-Wesley, 2nd edition, 2007.
- [4] Feng Xiao. *Measurement of the Radiative Muon Decay Branching Fraction in the MEG Experiment*. PhD thesis, University of California, Irvine, 2010.
- [5] David Griffiths. *Introduction to Elementary Particles*. Wiley-VCH, 2nd edition, 2008.
- [6] Y. Okada Y. Kuno. Muon decay and physics beyond the standard model. *Reviews of Modern Physics*, 73(1):151–202, 2001.
- [7] E. A. Kuraev E. Bartox and M. Secansky. Radiative corrections to muon decay in leading and next-to-leading approximation for electron spectrum. *Physics of Particles and Nuclei Letters*, 6(5):365–367, 2009.
- [8] A. Czarnecki A. Arbuzov and A. Gaponenko. Muon decay spectrum: Leading logarithmic approximation. *Physical Review D*, 65(113006), 2002.
- [9] William R. Leo. *Techniques for Nuclear and Particle Physics Experiments*. Springer-Verlag, 2nd edition, 1994.
- [10] K. A. Olive et al. 2014 review of particle physics. *Chin. Phys. C*, 38(090001), 2014.
- [11] R. M. Sternheimer. The density effect for the ionization loss in various materials. *Physical Review*, 88(4):851–859, 1952.

- [12] M. J. Berger W. H. Barkas. *Tables of Energy Losses and Ranges of Heavy Charged particles*, page 103. Number 39 in Nuclear Science Series. National Academy of Sciences, 1964.
- [13] S.M. Seltzer and M. J. Berger. Bremsstrahlung spectra from electron interactions with screened atomic nuclei and orbital electrons, 1985.
- [14] R.H. Pratt, H.K. Tseng, C.M. Lee, L. Kissel, C. MacCallum, and M. Riley. Bremsstrahlung energy spectra from electrons of kinetic energy  $t_1=1\text{-}2000$  kev incident on neutral atoms  $z=2\text{-}92$ , 1981.
- [15] B.J. McParland. *Medical Radiation Dosimetry*. Springer-Verlag, 2014.
- [16] L.D. Landau. On the energy loss of fast particles by ionization. *Journal of Experimental and Theoretical Physics (USSR)*, 8(201), 1944.
- [17] Glenn F. Knoll. *Radiation Detection and Measurement*. John Wiley and Sons, 2nd edition, 1989.
- [18] L. Urbán. *geant4 Physics Reference Manual*. CERN, 2014.
- [19] H.A. Bethe. Molière's theory of multiple scattering. *Physical Review*, 89(6):1256–1266, 1953.
- [20] S. Cecchini and M. Sioli. Cosmic ray muon physics. In R. A. Carrigan, editor, *Non-accelerator particle astrophysics: Proceedings*. Trieste University, 1998.
- [21] J. Beringer et al (Particle Data Group). Pdglive particle summary: Leptons. *Physical Review D*, 86(010001), 2012.
- [22] R. J Finkelstein R. E. Behrends and A. Sirlin. Radiative corrections to decay processes. *Physical Review*, 101(2):866–873, 1955.
- [23] S. Amuroso et al. Measurement of the mu decay spectrum with the icarus liquid argon tpc. *European Physics Journal*, C33:233–241, 2004.